Projection-Specific Intersectional Optogenetics for Precise Excitation and Inhibition in the Marmoset Brain

Luke Shaw[1], Krishnan Padmanabhan[1], Amy Buckleaw[1], Jude F. Mitchell[2,*], Kuan Hong Wang[1,3,*]

[1]Department of Neuroscience, Del Monte Institute for Neuroscience, University of Rochester Medical Center, Rochester, NY 14642, USA

[2]Department of Brain and Cognitive Sciences, University of Rochester, Rochester, NY 14611, USA

[3]Lead contact

[*]Correspondence:

jmitch27@ur.rochester.edu

Kuanhong_wang@urmc.rochester.edu

SUMMARY

The primate cerebral cortex relies on long-range connections to integrate information between functionally specialized areas. Investigating these processes requires tools that can selectively modulate specific projection pathways. While cell-class-specific optogenetics can modulate local circuits, these approaches often lack pathway specificity. Projection-specific optogenetics offers greater precision, especially in primates, where cortical areas are spatially and functionally well-separated. To address challenges in translating this approach from rodents to primates, we developed a mouse-to-marmoset pipeline. We first validated that optogenetic targeting of inhibitory neurons (AAV9-Dlx-ChR2) effectively silenced local cortical areas in marmosets. We then tested selective excitation and inhibition of defined projection pathways. By intersecting retrogradely delivered Cre-recombinase (AAVretro-Cre) with locally injected Cre-dependent opsins (AAV8-FLEx-ChR2 or Jaws), we achieved efficient, direction-specific labeling of both callosal and longitudinal projections. This intersectional strategy enabled precise excitatory and inhibitory control of cortical activity using distinct light wavelengths, advancing projection-specific optogenetics for investigating primate brain circuit function.

Keywords:

Intersectional optogenetics, marmosets, projection-specific, excitation and inhibition, adeno-associated virus, retrograde labeling, Cre recombinase, mDlx-enhancer, laminar recording

INTRODUCTION

The coordinated activity of the cerebral cortex relies on long-range connections that integrate the neural activity of specialized processing regions[1]. A fundamental challenge of neuroscience is to decipher the architecture of these brain circuits and their functional impacts on neural activity and behavior. The advent of optogenetics, a technique that enables precise manipulation of neural firing through specific wavelengths of light, has significantly advanced our understanding of targeted circuits and neuronal populations[2]. However, the adaptation of this powerful toolkit for use in non-human primate (NHP) studies has progressed more slowly compared to its application in rodent models[3,4].

Studies using non-human primate (NHP) models are essential for advancing our understanding of human brain circuits. Key features of NHP cortical architecture include larger brain sizes and extensive long-range neuronal projections that link functionally specialized cortical regions[5,6]. Compared to rodent neural architecture, NHP cortical areas are more functionally distinct and include elaborated intermediary processing regions, such as those in the frontal and parietal association cortices[7-9]. The common marmoset (*Callithrix jacchus*), a small, lissencephalic New World primate, is particularly valuable for translational neuroscience due to its cortical architecture, which closely resembles that of Old-World monkeys and apes while offering greater experimental accessibility and animal availability[10,11]. Furthermore, marmosets possess highly developed visual systems and exhibit cooperative social behaviors, making them particularly well-suited for functional and behavioral studies in primates[12-16]. Here, we used a mouse-to-marmoset pipeline to refine techniques used in mice to achieve cell-type and projection-specific optogenetic labeling and modulation in marmoset cortex.

Selective targeting of neural circuit components has been widely accessible in rodent models through the development of transgenic Cre-lines, which enable local injections of adeno associated virus (AAV) to express opsins restricted to Cre-labeled cell classes[17,18]. In contrast, comparable methods in NHPs have been significantly limited by the challenges of establishing stable transgenic Cre lines[3,19]. Although AAV-based opsin delivery reliably produces expression in NHPs[20-22], the resulting optogenetic stimulation effects are often weak or difficult to interpret[3,4,23]. One likely explanation for these suboptimal effects is that many of these studies utilized pan-neuronal promoters to achieve robust expression. The downside of this approach is that stimulation of pan-neuronal populations simultaneously affects excitatory and inhibitory cell classes, potentially cancelling each other's effects in local area. In addition, projections traversing the expression site are also likely to be affected. To limit the scope of expression, an inhibitory neuron-specific mDlx promoter has been used to drive ChR2 expression via AAV delivery[24]. This approach has shown reliable inactivation in both rodents and macaque monkeys[25-27]. It achieves optogenetic inactivation specifically in the area of AAV injection, as inhibitory neurons predominantly project locally within the cortex[28,29]. However, even this approach is still not specific in its effects on one cell class, as inhibition suppresses activity of all surrounding cells irrespective of their projection patterns.

To further target cortical neurons based on their projection pathways, the transport and diffusion of AAV-delivered opsins along long-range projections can be harnessed using a two-virus intersectional approach. This strategy, well-established in rodent studies[30-32], involves injecting an AAV-Cre engineered for retrograde transport (AAVretro-Cre)[33,34] at the termination of a projection, while simultaneously injecting an AAV carrying

a Cre-dependent opsin cassette at the projection origin. A key challenge in intersectional methods is selecting viral vectors that work synergistically to achieve high labeling specificity. Different AAV serotypes exhibit distinct cell entry locations and transport tropisms (retrograde or anterograde), which must be carefully matched[22,35,36]. While AAVretro is a clear and effective choice for retrograde transport at targeted terminals, the complementary virus injected at the site of the projection neuron's somas must be carefully chosen. This virus must exhibit low retrograde transport affinity to minimize off-target or "leaky" expression in circuits with reciprocal projection patterns, which is particularly critical in primate cortex, where bi-directional projections are common[6,22,37]. Additionally, optimizing the health and stability of transduced neural tissue requires careful testing of viral serotypes and particle concentrations[38,39], which can be difficult when animal numbers are limited.

To establish projection-specific intersectional optogenetics for precise excitation and inhibition in the primate brain, we conducted initial testing and titration of AAV vectors in mouse models before translating the approach to marmosets to ensure efficiency, specificity, and safety. One method that has been particularly effective to silence local cortical areas in both rodents and primates involves selective expression of ChR2 among inhibitory neurons under the mDlx promotor[25-27]. To validate this method in the marmoset cortex, we employed our AAV delivery and optogenetic methods in the premotor cortex and assessed cortical inactivation using electrophysiology. Consistent with previous studies, we find robust, though non-selective, suppression of local cortical populations. Having validated this technique in the marmoset cortex, we next sought to establish projection-specific intersectional optogenetics. We tested combinations of AAVretro with

either AAV9 or AAV8 in bilateral and longitudinal cortical projection pathways. AAV8 provided a better choice for pathway-specific expression while minimizing overexpression and leaky labeling. Furthermore, we tested the co-expression of the excitatory opsin ChR2 and the inhibitory opsin Jaws[40], demonstrating robust projection direction-specific expression in premotor and parietal pathways. Finally, two-color optogenetic excitation and inhibition in projection-specific neurons were validated using electrophysiology in the marmoset cortex. Together, these results provide powerful tools for the functional dissection of NHP cortical circuits.

RESULTS

Optogenetic methods offer incredible power to address fundamental neuroscience questions, however optogenetic experiments in NHPs present several challenges due to limited animal numbers and the genetic manipulations available. One method that could offer targeted manipulation and is well suited to the size and functional segregation of the primate brain is projection specific optogenetics. We implemented a mouse-to-marmoset pipeline to troubleshoot and optimize opsin delivery using various AAV serotypes, promoters, and a two-virus intersectional strategy designed to achieve expression in unidirectional projection pathways. We sought to characterize the expression efficiency and specificity and to further determine optogenetic stimulation effects in electrophysiology.

mDLX-ChR2-mediated Local Inhibition in the Marmoset Brain

To first validate our optogenetic preparation in marmoset cortex, we tested the use of mDlx-ChR2 for suppressing local cortical populations, a method that has proven robust

in other NHP preparations over recent years[24,25]. The use of mDlx-ChR2 offers area-specific control of cortical inhibition with millisecond response timescales and minimal invasiveness. To examine the labelling patterns and optogenetic effects of virally delivered mDlx-ChR2 in the marmoset, we injected AAV9-mDlx-ChR2 into the premotor cortex of a marmoset. After an expression period, we performed electrophysiological recordings while the animal was head-fixed, alert, and engaged in viewing natural images (**Figure 1A**). Viral micro-injections were delivered at 2-3 sites in a 3mm x 3mm craniotomy to maximize expression coverage over an area of cortex. Histological analysis confirmed robust labeling of mDlx-ChR2+ cells with inhibitory interneuron morphology (**Figure 1 B,C**). In the premotor cortex section with the highest amount of labeling, a total of 288 ChR2+ cells were identified. In this section, labeled somas and dendrites extended over an area of 3.67 mm^2, with a soma density of 78.47 cells/mm^2. Additional coronal sections located 0.5 mm anterior and 0.5mm posterior to this section were also quantified. These sections showed labeled cortical areas of 3.43 mm^2 and 3.52 mm^2, with corresponding soma densities of 74.34 cells/mm^2 and 73.58 cells/mm^2, respectively. The area of expression extended approximately 1.6 mm anterior and posterior to the central section before tapering off.

ChR2 delivery using the mDlx promoter has been shown to specifically target inhibitory interneurons[25]. Optogenetic stimulation using this construct stimulates inhibitory cells, which act to suppress local network activity due to their local inhibitory projections. Electrophysiological signatures of this stimulation should thus show two general trends: a small population of activated units, putative inhibitory mDlx+ labeled neurons that increase their firing rate under ChR2 stimulation, and a more sizeable population of

inhibited units whose firing rate drops off due to the activity of the excited inhibitory interneurons.

We tested if our preparation for recording and optogenetic stimulation would be sufficient to produce robust suppressive effects. We delivered light at the cortical surface through a thin layer of silastic protecting the underlying brain tissue. Spike sorted data from five recording experiments at different sites within the craniotomy were combined and analyzed as a function of light-triggered spike rate modulation and cortical depth. These experiments delivered 40 ms pulses of ChR2 light stimulation at a rate of 5 Hz in 30 second runs (16 mW, 470 nm: 127.32 mW/mm^2 at fiberoptic tip, estimated 38.2 mW/mm^2 at cortical surface). Over five recordings, a total of 279 unique units were identified with well isolated spike waveforms (see Methods). Eighty-one of these units showed modulation during the light activation period, with firing rates deviating above or below baseline by more than two times the standard error of the mean (SEM).

A subset of neurons showed excitation on ChR2 stimulation, consistent with characteristics of inhibitory interneurons, while the majority of neurons were suppressed. We examined the latency and direction of light triggered modulation timing as well as spike waveform characteristics of modulated units to determine whether they match the expected features of directly activated inhibitory cells or inhibited downstream cells. Due to the small size and short refractory period of typical inhibitory interneurons, we expect that a directly activated inhibitory cell should have spike waveform with short trough (T) to peak (P) duration as well as short peak to refractory half height (HH) duration[41,42]. A unit with such characteristics (**Figure 1D**) was identified, which also shows short latency activation within the laser-on period (**Figure 1E**). This unit's spiking activity first deviated

from baseline 3ms post-laser onset, which is typical of direct ChR2-mediated activation[2]. Further exploration of the population also showed units with spike waveforms of longer duration and longer half height refractory periods, typical of pyramidal cells (example, **Figure 1F**)[41,42]. One such broad spiking neuron was inhibited by light stimulation, and had a slower latency in its suppression (**Figure 1G**). The onset of this effect was 11ms, which follows from it being an indirect effect mediated by direct activation of an inhibitory neuron.

We found that the majority of cells showed a general trend of activity suppression in response to mDLX-ChR2 stimulation, while only a small subset were excited (**Figure 1H**). To illustrate this activity modulation on a population scale, identified units were grouped as excited or inhibited using a modulation index. This index was calculated by subtracting the baseline firing rate from the instantaneous firing rate (binned at one-millisecond resolution) and dividing the result by the sum of the instantaneous and baseline rates. Of the 279 units, 77 showed significant negative modulation and 4 showed significant positive modulation (**Figure 1I**). For this classification, we looked specifically at an early window of 10ms to 25ms to disregard slower network effects. As expected, when we separated the population of activated cells from the population of inhibited cells and examined the modulation onset times for these groups, the small subset of activated cells were significantly modulated within 5ms ($\bar{x}$=3.59ms, σ=.42), while inhibited cells were significantly modulated at slower latencies in a range of 3 to 15ms ($\bar{x}$=8.36ms, σ=.29) (**Figure 1J**). Analyses of spike waveforms demonstrated that excited units generally demonstrated characteristics of inhibitory interneurons, including narrow spike widths and short repolarization durations. When spiking waveform trough to peak

durations were plotted against peak to half height repolarization durations, three of the four activated units appeared within a cluster of short duration waveform features whereas the suppressed units appeared within a larger cluster with longer duration spiking features (**Figure 1K**).

In addition, we found that light modulation impacted neurons across cortical depths even though the optical fiber was placed above the silastic protecting the cortical surface. Of the activated units, the anatomically deepest unit was found at 1.45mm relative to the cortical surface. Of the inhibited units, the anatomically deepest unit was found at 1.98mm relative to the cortical surface, which is approximately the bottom extent of A6DC cortex.

In a separate control recording, we performed tests of laser power and wavelength to validate that suppression effects were not due to tissue heating and to further confirm that deep cortical layers could be modulated by light at the surface. First, a laser power reduction test confirmed that optogenetic modulation is concomitantly reduced. A total of 71 units were found in this series of recordings and are shown as heatmaps arranged by their depth relative to the cortical surface (**Figure 1L-M**). Using 16mW of blue light (470nm, 127.32mW/mm^2 at tip), we found consistent suppression of responses as deep as 1.0 mm, while at lower power of 8mW (470nm, 63.66mW/mm^2 at tip) the effects were more limited to a range between 0.30 to 0.80 mm**.** Further, we performed a wavelength control using 20mw green laser (561nm, 159.15mW/mm^2), which should minimally activate ChR2 but produce comparable tissue heating, and found no effects at any depth (**Figure 1N**). Additional tests were performed using 4mW blue light stimulation (470nm, 31.83mW/mm^2 at tip), which showed almost no suppression (**Supplemental Figure 1**). For all conditions, a mean modulation score across units in the 10ms to 40ms post laser

onset window was significant at 16, 8 and 4 mW blue light (two-tailed student's t-tests, 16mW: μ =-.73,p=8.3E-30; 8mW: μ =-.23,p=8.4E-16; 4mW: μ=-.10,p=6.5E-8), while the green light control and shuffled null control were non-significant as expected (Green: μ =.03, p=.086; Null: μ = -.02, p=.23). Finally, this experiment confirmed that in the higher power condition (16mW), stimulation from the cortical surface was sufficient to suppress activity even at the deepest sites at slight over 1mm of depth (**Figure 1L**).

AAV9-based Intersectional ChR2 Expression Lacks Specificity

To first test the efficacy of projection-direction-specific intersectional labelling in the marmoset, we utilized an AAV9 serotype to deliver CAG-FLEx-ChR2 to the cell bodies of cross-callosal projection cells in the right hemisphere of the premotor cortex, combined with AAVretro-hSyn-Cre injection in the left hemisphere (**Figure 2A**). AAV9 was our first choice due to the high efficiency of this serotype, which has been documented in marmoset cortex[7,22,43]. Left and right premotor cortex are connected by dense, bi-directional callosal projections [6,44] and thus this circuit served as an ideal ground for tests of a robust and relatively short-range projection.

Initial findings suggest that intersectional labeling with AAV9 yields highly efficient expression. This approach produced a generally symmetric labeling pattern across the cerebral hemispheres, with cross-callosal projections terminating in a columnar, patchy manner within bilaterally corresponding regions (**Figure 2B; Supplemental Figure 2**). However, dense parenchymal labeling made cell quantification challenging. Although labeling in the left hemisphere would be expected if limited to axonal terminals, the presence of numerous labeled cell bodies (**Figure 2C1–2**) suggests reduced specificity

and possible leakiness into the reciprocal projection pathway. Furthermore, some cortical areas showed signs of overexpression, evidenced by the accumulation of labeled puncta in dendritic arbors and somas (**Figure 2C3–5**), whereas other regions displayed healthy expression characterized by uniform membrane labeling (**Figure 2C1, 2, 6**).

To quantify the extent of expression in each hemisphere, we used an automated tissue classification approach based on the tunable artificial neural network (ANN) supplied in QuPath software. This approach enabled classification of epifluorescence images across the entire sectioned brain, with sampling at one section every 300 um. The ANN was trained to discriminate healthy expression (yellow), over-expression expression (red), and un-labelled tissue (**Figure 2D**). Training sets included examples of labelled axon tracks, terminal fields, and cell bodies. Notably, the extent of labelling, shown as the percentage of tissue area covered by labels, was widespread in both hemispheres with higher incidences of overexpression in the right hemisphere (**Figure 2E**). Regions of overexpression in the right hemisphere spread 4 millimeters over the anterior/posterior coordinate frame and are also detected in the left hemisphere close to the injection site.

AAV9's high transduction efficiency and endogenous retrograde transport properties[22,35,45] contributed to off-target labelling not only at the Cre injection site in the left cortex, but also in the thalamus. While labeling of descending cortical projections (**Figure 2F**) and terminal fields in subcortical structures (**Figure 2D**) was expected, we also observed extensive cell body labelling in the right Ventral Anterior Lateral (VAL) thalamus (**Figure 2G**), a motor-related region known to project to the premotor cortex. This unexpected expression pattern may result from retrograde transport of both AAVretro and AAV9 in VAL-originating projections that ascend to the right premotor

cortex and decussate to the left premotor cortex via the corpus callosum. Similar decussating thalamo-cortical labelling patterns have been reported in frontal cortical areas of macaques[46], as well as in mice[47] and rats[48]. While informative, such off-target labeling compromises projection specificity. To address this, we tested alternate AAV serotypes in the mouse to further improve labeling precision.

Testing Intersectional ChR2 and Jaws Co-Expression using AAV8 in the Mouse

A wide range of AAV serotypes, promoters, and viral titers can be used in combination with AAVretro to achieve intersectional labeling of a single projection direction, though their efficacy and specificity can vary considerably. Most studies using these tools in mice[22,49-51] employ significant numbers of test animals to pilot different serotype, promoter, and titer combinations to optimize the desired expression properties. However, in non-human primates the numbers of animals for use can often be limited. This challenge for viral optimization became apparent in our first test in marmoset cortex, detailed above, where we found AAV9 led to overexpression and leaky expression in the reciprocal projection pathway. Our findings highlight the need to optimize viral parameters using multiple test animals, ultimately including mice as well as marmosets.

To achieve more specific labelling of targeted projections, we tested in the mouse an AAV8 serotype with less retrograde affinity in an effort to eliminate leaky expression in the reciprocal pathway to obtain better directional specificity. In addition, we tested the feasibility of including not only the excitatory opsin ChR2 but also of the inhibitory optogenetic chloride pump Jaws to suppress the projection pathway[40]. AAV8 was

selected because comparative analyses of AAV serotype expression profiles indicated that AAV8 demonstrates a more balanced cortical expression profile, providing efficient local transduction while avoiding excessive retrograde transport[34,35]. We again used a cross-callosal injection strategy, delivering AAVretro-hSyn-Cre-BFP into the left M1/M2 region and a 1:1 mixture of AAV8-CAG-FLEx-ChR2-tdTomato and AAV8-CAG-FLEx-Jaws-GFP into the right M1/M2 (**Figure 3A**).

One advantage in using mice for these tests is that it is possible to perform a larger number of controls with test animals. In total we used 26 mice to optimize this strategy with AAV8, to test alternate serotypes, and to validate optogenetic stimulation in electrophysiology. We first performed a test using the AAV8 vectors to confirm there was no expression of ChR2 in the absence of Cre, which might occur due to spontaneous recombination reverting FLEx-ChR2. This was performed using a 1:1 mixture of the AAV8-FLEx-ChR2/Jaws vectors injected into the M1 cortex. Our tests indeed showed no identified Cre-independent expression from the AAV8 vectors (**Figure 3B**).

We also examined if poor tissue health and over-expression could be mitigated by adjusting the dilution of the AAV solution. AAV injection-related cytotoxicity can result from excessively high viral titers or residual cytotoxins from the production process. Diluting the viral solution effectively reduces the risk associated with both factors. We first tested a fresh batch of virus without dilution. A total of 400 nL of a 1:1 mixture of AAV8-CAG-FLEx-ChR2 (3E13 gc/mL) and AAV8-CAG-FLEx-Jaws (5E13 gc/mL) was injected into the right M1 cortex, while AAVretro-hSyn-Cre (1E14 gc/mL) was injected into the contralateral M1 cortex. The virus injection site showed poor tissue health and a lack of expression at the center (**Figure 3C**, center of dashed rectangle), with stronger

expression observed in the surrounding tissue. This pattern prompted us to perform dilution experiments. We found that a 1:1 mixture of AAV8-CAG-FLEx-ChR2 diluted 1:2 (final titer: 1E13 gc/mL) and AAV8-CAG-FLEx-Jaws diluted 1:5 (final titer: 1E13 gc/mL) was sufficient to prevent cytotoxicity while maintaining adequate expression levels (**Figure 3D, right hemisphere)**.

Having optimized the viral dilution, we performed head-fixed, awake electrophysiological recordings to test if co-expression of Jaws and ChR2 enabled robust suppression and excitation of the callosal projection. To test the effects of ChR2 stimulation and combined ChR2 and Jaws stimulation, we delivered trains of 5Hz, 50ms pulses using a 470 nm laser (159.15 mW/mm^2 at the tip) for ChR2 activation, concurrently with overlapping 0.5 Hz, 1-second pulses of 561 nm light (159.15 mW/mm^2 at the tip) for Jaws activation (**Figure 3E**). Optical stimulation was delivered by a fiber-optic cannula placed directly above the brain surface and recordings were performed with a 64-channel multielectrode array at the AAV8 injection site where the cell bodies of projection neurons were labeled. Neural spiking activity was identified on each recording channel and peri-stimulus time histograms were generated for laser pulse events. A clear time-locked increase in firing rate was observed in response to ChR2 stimulation events in an example unit (**Figure 3F**). However, in the same unit, this response was greatly reduced when ChR2 stimulation events occurred during Jaws stimulation events (**Figure 3G**). These effects were also evident in local field potential (LFP) recordings across the population of channels, reflected by a reduction in the mean negative deflection (**Figure 3H,** shown with 1x SEM error fields). The peak voltage deflection induced by ChR2 stimulation was reduced by 72.1% during concurrent Jaws stimulation. These findings indicate both the

co-expression of Jaws and ChR2 in recorded units and the ability of Jaws stimulation to suppress ChR2 driven neural spiking activity. Having demonstrated efficient and specific intersectional co-expression of ChR2 and Jaws using AAV8 in the mouse, we next translated this approach to the marmoset.

Intersectional AAV8-Mediated ChR2 and Jaws Co-Expression in the Marmoset Premotor Callosal Projections

Applying AAV8 for intersectional co-expression of ChR2 and Jaws in marmoset cortex resulted in greater specificity than AAV9 for targeting the cross-callosal projection. Using dilutions established from mouse testing, we injected AAVretro-hSyn-Cre-BFP into the left premotor/motor cortex (A6DC/A4) and a 1:1 mixture of AAV8-CAG-FLEx-ChR2-tdTomato and AAV8-CAG-FLEx-Jaws-GFP into the right premotor/motor cortex (**Figure 4A**). This approach produced robust and widespread expression at the AAV8 injection site, spanning approximately 2.5 mm mediolaterally at the peak (**Figure 4B,C**), with labeling in both superficial and deep layers consistent with the distribution of callosal projection neurons. The observed patchy expression pattern may reflect a combination of the injection strategy, which involved two separate 1.5 µL injections per hemisphere at two depths, and the specific connectivity of the intersected projection. Tissue disruption from subsequent electrophysiological recordings may also contribute to this pattern (**Supplemental Figure 3**). Importantly, unlike prior high-titer AAV8 injections (**Figure 3C**), this expression was not associated with a loss of healthy neurons within the injection site. Morphological analysis confirmed healthy cell bodies and dendritic arbors with clear co-expression of ChR2 and Jaws (**Figure 4D**, circles).

Manual cell counting revealed robust on-target expression in the right cortex and minimal off-target expression in the left cortex, based on epifluorescence images across the anterior-posterior axis (**Figure 4E**). At the expression peak (+10.4 mm A/P) in the right cortex, 378 Jaws+, 91 ChR2+, and 54 co-expressing cell bodies were identified, corresponding to 14.3% co-expression within the Jaws+ population and 59.3% within the ChR2+ population. In contrast, the left cortex at the same coordinate showed only 26 Jaws+ and 3 ChR2+ cell bodies, along with terminal field labeling in both channels (**Figure 4F**). The expression area in the right cortex extended ~3 mm along the A/P axis—more focal than the broader spread (~6 mm) seen with AAV9 (**Figure 2E**). Despite the higher number of Jaws+ somas, labeled Jaws+ axons exiting the region were notably fewer compared to $ChR2^{+}$ axons (**Supplemental Figure 4**). Off-target expression in the thalamus was also substantially reduced, with only two labeled cell bodies observed in the right ventral anterior thalamus, aside from expected axonal labeling (**Figure 4G**). Thus, although AAV8 resulted in moderately lower overall expression efficiency than AAV9, it avoided overexpression-related fluorescence accumulation and significantly reduced off-target and leaky labeling, supporting its suitability for projection-specific targeting.

Intersectional AAV8-Mediated ChR2 and Jaws Co-Expression in Marmoset Premotor–Parietal Projections

While tests in cross-callosal projections in premotor cortex validated viral efficiency and specificity, we also sought to test this method in a longer-range cortico-cortical projection pathway. We selected a feedback projection from A6DR in premotor cortex to

the medial intraparietal area (MIP) in parietal cortex for testing, which is an ipsilateral projection that traverses 13 mm of cortex along the anterior/posterior axis and contains robust feedforward and feedback interconnectivity. Using the same injection strategy as in the cross-callosal experiment above, we injected AAVretro-hSyn-Cre-BFP into the right parietal cortex and a 1:1 mixture of AAV8-CAG-FLEx-ChR2-tdTomato and AAV8-CAG-FLEx-Jaws-GFP into the right premotor cortex (**Figure 5A**).

Consistent with the previous callosal tests, the AAV8 intersection strategy achieved efficient transduction and high specificity for this longer-range frontal-parietal projection. To verify injection sites and assess labeling specificity, we performed manual cell counting to map the 2D positions of labeled Cre+ cells in the parietal cortex and ChR2+/Jaws+ cells in both parietal and premotor cortices, enabling estimation of on-target and off-target labeling (**Figure 5B,C**). Quantification at the premotor site included 15 coronal sections sampled at 0.3 mm intervals, which spanned 5 mm of brain tissue along the A/P axis. A total of 137 Jaws+ cells, 37 ChR2+ cells, and 31 co-expressing cells were counted at the section containing maximum labeling (A/P +12.85 mm, A6DR) (**Figure 5D**). This was equivalent to 22% co-expression in the Jaws+ population and 83.8% co-expression in the ChR2+ population. While cells were counted at all sampled sections, the main area of expression extended from +11.35mm to +13.45mm. Qualitatively, labelled cells at the premotor injection site (**Figure 5E**) showed characteristic patterns of healthy expression, with Jaws+ cell bodies appearing more well-defined (**Figure 5F,H**) than those labeled with ChR2. Despite less distinguishable somatic labeling in the ChR2 channel, dense labeling of dendritic processes was still evident (**Figure 5G,H**). An additional feature of expression in the premotor area was the presence

of clustered labelled contralateral terminals, suggesting that this population of neurons projecting to the parietal cortex also sends axon collaterals to contralateral premotor areas and more anterior ipsilateral areas (**Supplemental Figure 5**).

We observed high specificity in targeting the projection from premotor to parietal cortex, as indicated by soma labeling restricted to the premotor cortex, with a relative absence of labeled somas in the parietal cortex (**Figure 5D**). To quantify this, 50 µm coronal sections were sampled at 0.5 mm intervals spanning +0.5 to +4.5 mm A/P. At the parietal injection site, very few labeled cells were detected, suggesting minimal off-target expression in the reciprocal projection pathway. Within a 2 mm range centered on the peak of Cre+ expression at A/P +1.8 mm (intraparietal sulcus areas), only one ChR2+ cell and one Jaws+ cell were found. Slightly anterior in parietal Area PE (+3 to +4.5 mm A/P), five Jaws+ and three ChR2+ cells were identified (**Figure 5D**). Imaging at the parietal injection site (**Figure 5I**) revealed dense ChR2+ axon terminal labeling in cortical layers 1 and 5/6 (**Figure 5J**), consistent with the laminar targeting of feedback projections. Notably, Jaws+ axon terminal labeling was absent (**Figure 5K**), suggesting that ChR2 is more efficiently transported into long-range axons than Jaws. This pattern persisted in anterior parietal areas. Although a few cell bodies were detected in these regions (**Figure 5L**), suggesting limited expression leakage in the reverse direction, quantification confirmed that off-target labeling was minimal, accounting for less than 1% of labeled cells (1 of 177 ChR2+ and 5 of 546 Jaws+ cells in the parietal cortex).

To assess the stability and reliability of expression over extended time periods, we repeated the experiment and extended the typical 1.5-month expression window to 8.5 months. This was performed using the same premotor and parietal injection sites, but

with ChR2 alone. Histological analysis and cell counting revealed healthy expression in the premotor cortex, with an increased number of labeled ChR2+ cells at the expression peak (113 cells), potentially due to the absence of competition with Jaws. However, this preparation also showed a proportionally higher number of labeled cells in the parietal cortex (peak = 34), indicating increased off-target expression (**Supplemental Figure 6**). Quantification across sections sampled at 0.3 mm intervals showed a mean of 90.37 ChR2+ cells (SEM = 7.84) in the 1.5 mm region surrounding the expression peak in premotor area A6DR (+12.1 to +13.6 mm A/P). In the parietal cortex (+0 to +5 mm A/P), a mean of 8.47 ChR2+ cells (SEM = 2.32) were counted. Overall, the proportion of off-target expression increased to 15% (129 of 754 total ChR2+ cells), compared to just 1% at 1.5 months. These findings suggest that extended expression durations may amplify expression leakage that remains undetectable at earlier time points.

Excitation and Inhibition of Specific Projection Neurons via Intersectional Optogenetics in the Marmoset

While the intersectional strategy produced clear and specific expression patterns in histological analyses, further validation was necessary to determine whether this level of expression was sufficient to modulate neuronal activity *in vivo*. To move beyond anatomical characterization and assess functional efficacy, we tested the excitatory and inhibitory effects of this intersectional labeling approach through in vivo electrophysiology. Recordings were performed in an anesthetized marmoset with cross-callosal co-expression of ChR2 and Jaws (**Figure 4**). Optical stimulation followed a protocol similar to that used in mice: 5 Hz, 40 ms ChR2 pulses (470 nm, 127.32 mW/mm² at tip) were

delivered to the cortical surface, along with simultaneous 1 Hz, 400 ms Jaws pulses (561 nm, 159.15 mW/mm²; **Figure 6A**). To improve the yield of spontaneously active units, we used a combined dexmedetomidine and isoflurane anesthesia protocol (see **Methods**), allowing for reduced isoflurane concentrations. Electrophysiological signals were filtered and spike-sorted to identify units showing optogenetically modulated firing rates.

A subset of neurons, presumed to be neurons projecting to the contralateral premotor cortex, exhibited clear responses to optogenetic stimulation. The extent of suppression by Jaws co-stimulation varied across units, ranging from no suppression to nearly 50%. One example unit showed short-latency, laser-triggered activation consistent with direct ChR2-driven excitation, but its firing remained unaffected during concurrent Jaws stimulation (**Figure 6B–D**). By contrast, another unit displayed ~50% suppression of ChR2-evoked firing during simultaneous Jaws stimulation (**Figure 6E–G**). Time-locking this unit's activity to the 400 ms Jaws stimulation pulses alone also revealed clear suppression of firing rate (**Figure 6H**). Out of 67 units recorded in a single session, 10 showed significant modulation of ChR2-evoked firing above 1 Hz. Population-level responses are summarized using a modulation score as described previously (**Figure 6I**). Analysis by cortical depth revealed modulated units at the deepest extent of the electrode array, confirming successful activation of projection neurons located in deep layers despite surface laser stimulation (1.1 mm; **Supplemental Figure 7**). Among the 10 ChR2-responsive units, four were significantly suppressed by concurrent Jaws stimulation, while none showed significant excitation ($p < 0.05$, two-sample, two-tailed t-tests comparing firing rates during ChR2 vs. ChR2+Jaws within a 5–45 ms window post-ChR2 onset;

Figure 6J). These suppressive effects were also reflected in the local field potential (LFP). A comparison of mean LFP traces showed a 59% reduction in the ChR2-evoked peak voltage deflection post-laser onset during concurrent Jaws activation (**Figure 6K**). Although the number of modulated neurons was small, as expected given the low proportion of callosal projection neurons in the population, these results confirm effective ChR2-mediated excitation and partial suppression by Jaws in targeted projection pathways.

Discussion

Successful application of optogenetic techniques in non-human primates (NHPs) remains a major challenge, particularly with respect to achieving selective expression in specific cell types or projection pathways. In this study, we optimized viral delivery strategies to achieve highly specific optogenetic modulation restricted to a cortico-cortical projection pathway in the common marmoset. We first validated our optogenetic preparation by replicating a well-established inhibitory approach previously used in macaques to induce behavioral deficits[24,25]. Using the mDlx promoter to drive ChR2 expression in inhibitory interneurons, we confirmed that surface cortical stimulation suppressed local neural activity. Spike waveform analyses further indicated activation of deep-layer inhibitory interneurons. Next, we developed and optimized an intersectional strategy for projection-specific targeting in marmoset cortex, using both mouse and marmoset models to identify optimal AAV serotypes and titers. This approach enabled target-specific expression in both shorter-range callosal projections between left and right premotor cortices and longer-range frontal-to-parietal projections within a hemisphere. Moreover, we successfully co-expressed two opsins, ChR2 for excitation and Jaws for

inhibition, within the same population of projection neurons. Following optimization, this strategy yielded stable, healthy expression in marmoset cortical tissue. Electrophysiological recordings confirmed that the intersectional approach produced sufficient expression to drive optogenetic modulation of neural activity *in vivo*.

Optimizing viral expression methods to enhance targeting specificity without compromising efficiency is essential for functional neuroscience experiments. Without conditional expression strategies like those described here, low specificity can result in modulation of heterogeneous neural populations, comprising mixed cell types and projection targets, which complicates interpretation. For example, expressing an excitatory opsin such as ChR2 using a highly efficient virus like AAV9 combined with a strong pan-neuronal promoter results in widespread labeling of local, retrograde, and anterograde projections. This leads to ChR2 expression across a broad range of local and projection neurons. Under standard optical stimulation, it becomes impossible to selectively activate only the projection neurons of interest without concurrently stimulating interneurons, inducing antidromic spikes, and triggering widespread, mixed network effects. Classical approaches, including microelectrode stimulation, pharmacological modulation, surgical lesions, and cortical cooling, suffer from similar limitations. Recent innovations, such as soma-targeting sequences, can reduce axonal activation and antidromic firing in distantly labeled neurons[52]. Additionally, 3D optical targeting strategies using multiphoton excitation offer enhanced spatial control[53]. However, these methods remain incomplete solutions or involve significant technical challenges. Given the current lack of transgenic Cre-driver lines in non-human primates, two-virus intersectional strategies represent one of the most effective available tools for achieving projection-

specific targeting, enabling the functional dissection of defined neural circuits in the primate brain.

To optimize intersectional viral expression, we first conducted testing in mice before proceeding to marmosets. Each viral batch was initially evaluated in the mouse, allowing for preliminary screening of injection parameters and the identification of key methodological adjustments. Notably, we found that dilution of the locally injected AAV8 virus was necessary to prevent overexpression. This dilution likely reduced the concentration of residual cytotoxic components from the viral preparation process and/or limited the number of viral particles entering each cell, which may otherwise impose metabolic stress at high concentrations[54]. This step proved critical, both for refining our procedures and for reducing the number of marmosets required for the study. Moreover, the mouse-based screening allowed us to compare multiple AAV serotypes and ultimately identify AAV8 as the most suitable candidate due to its lower retrograde transport affinity, which minimized off-target expression in the reciprocal projection pathway.

Translating intersectional methods to the marmoset model required further adjustments to our injection strategy to accommodate the species' larger brain size and anatomical variability. This variability, well-documented across individuals, poses a particular challenge for stereotaxic targeting in the absence of MRI guidance[55]. To increase the likelihood of targeting the intended regions, we distributed injections across multiple sites within each craniotomy. Additionally, higher injection volumes and multiple depth penetrations were used to minimize issues such as backflow and uneven viral distribution. An interesting source of variability observed in both AAV8 experiments was the differing number of Jaws-expressing versus ChR2-expressing cells. One possible

explanation is viral competition, in which infection by one vector may reduce the efficiency of co-infection by the second, thereby decreasing the rate of co-expression. Alternatively, the potassium channel trafficking motifs included in the engineered Jaws construct may preferentially localize expression near the soma[40,56,57], potentially biasing detection in cell counts.

While AAV9 demonstrated high transduction efficiency in our initial intersectional tests, consistent with previous reports[35], it also produced leaky labeling, likely due to its known retrograde transport affinity[36,45]. A prominent finding was the abundance of off-target soma labeling in the left cortex and in the motor thalamus, relative to the targeted right cortex. Although anterograde trans-synaptic transport has been reported for AAV1 and AAV9[58], to our knowledge, this property has not yet been documented for AAVretro. Alternatively, the thalamic labeling may result from retrograde transduction by both AAVretro and AAV9 in thalamic neurons that project to the right premotor cortex and also send decussating axons to the left premotor cortex. Such decussating thalamo-cortical projections have been described in the rat[48], hedgehog[59], and macaque[46]. Importantly, our data suggest that AAV9 can still be used effectively without overexpression when paired with cell-type-specific promoters. For example, when combined with the inhibitory neuron-specific mDlx promoter, AAV9 yielded healthy, specific labeling that remained stable for at least 10 months. These results indicate that, despite its limitations, AAV9 remains a useful tool, particularly when used with promoters that produce moderate expression in defined neuronal populations.

The application of mDlx-ChR2 in the marmoset cortex confirmed its utility for silencing activity within a local cortical area. Previous studies in macaques have used

mDlx-driven optogenetics to achieve cortical inhibition and demonstrated robust electrophysiological inactivation in primary visual cortex (V1), with modulation profiles closely resembling those observed in our current results[25]. Our findings contribute two important advances to ongoing research on mDlx-mediated optogenetics. First, we employed a noninvasive method of surface illumination through a silastic-protected cranial window. Combined with single-unit spike waveform analysis, this approach enabled the detection of inhibitory interneuron activation at depths of up to 1.1 mm from the cortical surface. This demonstrates the feasibility of noninvasive optogenetic activation of deep-layer neurons, which is particularly valuable for experiments not involving invasive optical delivery. Second, our study extends the use of mDlx-ChR2 to the premotor cortex—a region with fundamentally different laminar architecture from V1. In contrast to the laminar-specific expression pattern previously observed in macaque V1, including a clear absence in Layer IV, our results showed no discernible laminar bias in premotor cortex. This difference likely reflects both regional and species-specific variability in interneuron distribution and viral expression. Further comparative studies will be needed to fully characterize these factors.

The direct excitatory and inhibitory optogenetic methods explored in this study achieve high labeling specificity through a viral intersection strategy; however, this approach has certain limitations. When targeting long-range projections, stimulation at axon terminals can help avoid off-target effects associated with optical stimulation at the injection site. For example, a study of feedback projections from the frontal eye field in macaques successfully achieved such specificity by stimulating projection terminals with the inhibitory opsin eNpHR3.0[60]. This approach, however, requires robust expression

throughout the entire projection pathway, an essential criterion that was clearly met by ChR2 in our experiments, but not consistently by Jaws. In the premotor-parietal projection, we observed no Jaws-positive labeling in the parietal cortex. Although Jaws-positive terminals were present in the premotor cross-callosal projection, their expression appeared less robust than that of ChR2. These observations suggest that Jaws is less efficiently transported to, or incorporated into, distal axonal membranes. A recent study employing Jaws-mediated terminal inhibition in a macaque V4-to-V1 feedback projection demonstrated functional inhibition via electrophysiology[61], but did not provide histological characterization of Jaws expression at terminals, leaving unresolved the question of its transport and localization efficiency in long-range projections. It is possible that inherent features of the Jaws construct limit its effectiveness in distal axons, warranting pathway-specific testing to determine suitability for terminal inhibition. Alternative tools, such as eNpHR3.0 or opto-GPCR-based inhibitory systems[62] that suppress synaptic transmission, may offer more reliable options for long-range projection targeting and should be considered to overcome this limitation.

While the co-expression and two-color optogenetic approach used in this study enabled simultaneous excitatory and inhibitory modulation in the anesthetized marmoset, there is room for improvement in the co-injection strategy. Jaws has previously been applied successfully in primate studies for site-specific inhibition, including in the superior colliculus[63] and area MT[26]. Similarly, ChR2 has seen broad application in primate optogenetics, from evoking forelimb movements via M1 stimulation[64,65] to modulating reward signaling in an amygdala–substantia nigra circuit[66]. In our preliminary mouse experiments, Jaws effectively suppressed ChR2-driven activity, with some units showing

near-complete inhibition. In contrast, the suppression observed in the marmoset was more subtle. One potential explanation is competition between the ChR2 and Jaws vectors for expression within the same neurons. As shown in our histological data and electrophysiological recordings, co-expression was not always well matched across cells, suggesting that complete bidirectional optogenetic control is not reliably achieved with this dual-virus method at the single neuron level. Given the likelihood of viral competition, a promising alternative is the use of a single opsin construct that combines excitatory and inhibitory components into a single molecule. One such tool, BiPOLES[67], enables bidirectional modulation via dual-wavelength stimulation and may offer a more reliable and efficient solution for future studies.

The intersectional optogenetic methods described here expand the growing toolkit available for primate optogenetics. To date, much of the field has focused on well-characterized or predominantly unidirectional circuits, such as those in the frontal eye fields[68], superior colliculus[63,69], and motor cortex[64]. By employing a viral intersection strategy, our approach enables the selective targeting of individual components within complex, integrative cortical circuits, such as those found in associative areas, with minimal off-target expression. These findings also highlight the utility of multi-color optogenetics, particularly when combined with cell type–specific tools. Used in tandem, these approaches allow researchers to replicate the functional outcomes of classical perturbation techniques, such as cortical cooling or muscimol injection, but with the added temporal precision and specificity of optogenetics. Moreover, selective projection inhibition from a defined source area offers a powerful contrast to local inactivation, helping to disentangle circuit-level contributions to behavior and physiology. Importantly,

this work also validates a minimally invasive method for delivering light through a cortical window in the primate brain, further broadening the methodological options for chronic or awake preparations. Together, these results demonstrate the feasibility of selectively targeting projection pathways between reciprocally connected cortical areas in primates and provide a robust framework for probing their causal role in brain function.

METHODS AND MATERIALS

Animal Use

All experimental protocols were approved by the University of Rochester Institutional Animal Care and Use Committee and were conducted in compliance with the National Institutes of Health guidelines for animal research.

Twenty-six wild type C57BL/6J mice were used for this study. Twenty (12 female, 8 male) were used for virus injection and histology alone. Three (3 male) were used for virus injection, anaesthetized terminal electrophysiology recordings, and histology. Three (3 female) were used for virus injection, awake head-fixed electrophysiology on a run wheel, and histology. Subjects were group housed at the University of Rochester Medical Center with a circadian cycle of 12-hour light and 12-hour dark. All subjects had full access to food and water at all times.

Five adult common marmosets (Callithrix jacchus) were used for this study. Marmoset S (male) and Marmoset X (female) were used for virus injection and histology alone. Marmoset Y (female) and Marmoset K (female) were used for virus injection, a terminal anaesthetized electrophysiology recording, and histology. Marmoset A (male) was used for virus injection, awake, head-fixed electrophysiology recordings, and histology. A summary of these experiments is provided in Table 1. Subjects were group housed at the University of Rochester with a circadian cycle of 12-hour light and 12-hour dark. All subjects had full access to food and water at all times.

Table 1 Marmoset Injection Procedures

Marmo	Virus	Original Titer	Injection Titer	Volume	Injection Target	Expression Peak	Expr Time
A (M)	AAV2/9-mMDLX-ChR2-mCherry	1.0E+13 gc/mL	1.0E+13 gc/mL	2x 1.5uL	Premotor A6DR +13AP, +5LR (right)	A6DC/A4 +10.8 AP, +5LR	10 months
A	AAV2/9-mMDLX-ChR2-mCherry	1.0E+13 gc/mL	1.0E+13 gc/mL	2x 1.5uL	Parietal Cortex MIP +0AP, +4LR	Parietal Area PE +4.15AP, +4LR	10 months
X (F)	AAV2/retro-hsyn.HI.GFP-Cre	1.17E+13 gc/mL	1.17E+13 gc/mL	2x 1.5uL	Premotor A6DC +12AP, -5LR (left)	A6DC +11.8 AP, -5LR	2 months
X	AAV2/9-CAG-FLEx-ChR2-TdTomato	8.32E+12 gc/mL	8.32E+12 gc/mL	2x 1.5uL	Premotor A6DC +12AP, +5LR (right)	A6DC +11.8 AP, +5LR	2 months
S (M)	AAV2/retro-pmSyn1-EBFP-Cre	1.04E+14 gc/mL	1E+13 Gc/mL	2x 1.5uL	Parietal Cortex MIP +0AP, +4LR	IPS – MIP/LIP/VIP +1.4AP, +4LR	1.5 months
S	AAV2/8-CAG-FLEx-Jaws-KGC-GFP-ER2	5.07E+13 gc/mL	5E+12 gc/mL	2x 0.75uL	Premotor A6DR +13AP, +5LR (right – co-injected)	A6DR +12.8 AP, +5LR	1.5 months
S	AAV2/8-CAG-FLEx-ChR2-tdtomato	2.0E+13 gc/mL	5E+12 gc/mL	2x 0.75uL	Premotor A6DR +13AP, +5LR (right – co-injected)	A6DR +12.8 AP, +5LR	1.5 months
Y (F)	AAV2/retro-pmSyn1-EBFP-Cre	1.04E+14 gc/ml	1E+13 Gc/mL	2x 1.5uL	Parietal Cortex MIP +0AP, +4LR	Parietal Area PE +3.3AP, +3LR	8.5 months
Y	AAV2/8-CAG-FLEx-ChR2-tdtomato	2.0E+13 gc/mL	5E+12 gc/mL	2x 0.75uL	Premotor A6DR +13AP, +5LR (right)	A6DC/A6DR Border	8.5 months
K (F)	AAV2/retro-pmSyn1-EBFP-Cre	1.04E+14 gc/ml	1E+13 Gc/mL	2x 1.5uL	Premotor A6DC +12AP, -5LR (left)	A6DC/A4 +10.7 AP, -5LR	2 months
K	AAV2/8-CAG-FLEx-Jaws-KGC-GFP-ER2	5.07E+13 gc/mL	5E+12 gc/mL	2x 0.75uL	Premotor A6DC +12AP, +5LR (right – co-injected)	A6DC/A4 +10.7 AP, +5LR	2 months
K	AAV2/8-CAG-FLEx-ChR2-tdtomato	2.0E+13 gc/mL	5E+12 gc/mL	2x 0.75uL	Premotor A6DC +12AP, +5LR (right – co-injected)	A6DC/A4 Border +10.7 AP, +5LR	2 months

Virus	Plasmid Manufacture	Virus Manufacture
AAVretro-hsyn-cre-GFP	Addgene	Addgene #105540-AAVrg
AAV2/retro-pmSyn1-EBFP-Cre	Addgene #51507	Boston Children's Hospital (BCH) Viral Core
AAV2/9-CAG-ChR2-tdtomato	BCH Viral Core	BCH Viral Core
AAV2/8-CAG-ChR2-tdtomato	Addgene #18917	BCH Viral Core
AAV2/8-CAG-FLEx-Jaws-KGC-GFP-ER2	Addgene #84445	BCH Viral Core
AAV2/9-MDLX-ChR2	Addgene	Addgene #83898-AAV9

Table 2 Viral Materials

Marmoset Injection Surgery

Prior to surgery, a final virus solution was prepared by mixing sterile saline with undiluted virus aliquots to achieve titers described in Table 1. Note that for co-injected virus (e.g. Jaws and ChR2), individual virus solutions were diluted to 1E+13 genomic copies per mL (gc/mL) and then mixed 1:1 in the final injected solution.

Prior to viral injection surgery, marmoset research subjects were anaesthetized with intramuscular injection of Ketamine and Midazolam followed by isoflurane delivery using a full-face mask prior to endotracheal intubation. After intubation, anesthesia was

maintained using 1.5-3% isoflurane while monitoring blood oxygenation, heart rate, rectal temperature, and respiration. The head was fixed to a Kopf stereotaxic frame using ear bars and a Kopf Model 916 Guinea Pig adaptor nose and tooth bar assembly. The head was positioned on the tooth bar to distribute pressure over the left and right sides of the dental arch. The head was rotated about the ear bars such that the plane formed by the lower orbits and the ear bars was parallel to the base of the stereotaxic frame. A stereotaxic arm was fixed to the frame and calibrated to align the x and y planes with respect to the ear bars to mark stereotaxic coordinates. An incision was made in the scalp and tissue was cleared at the skull surface. Injection target locations were marked on the skull (Premotor-Premotor: 10mm anterior to intra-aural (IA) line, 4mm left and right of midline; Premotor-Parietal: 10mm and 0mm anterior to IA, 4mm right of midline). 3mm moat craniotomies were drilled at each target site. The skull chip was removed, and craniotomy edges were smoothed with a coarse Dremel bit.

Two injection site targets were identified within each craniotomy based on the pattern of vasculature. A small slit was made in the dura at each target. A Nanoject III (Drummond Scientific) was set to inject 3 quantities of 500nL of viral solution at each dural slit at cortical depths of 1.5mm, 1mm, and .5mm. The injection rate was set to 2nL/second. Two minutes were allowed to pass before the beginning of each injection and after the end of each depth injection. After injection, craniotomies were sealed with a thin layer of bone wax and the skin was sutured following the administration of slow-release analgesic for post operative recovery. A minimum expression period of 6 weeks elapsed prior to sacrifice for histology or electrophysiology experiments. Further experimental details for individual animals are documented in Table 1.

Marmoset Head Implant and Injection Surgery

Marmoset A was surgically implanted with a head cap and recoding chambers for awake, head-fixed optogenetic stimulation and electrophysiology. Two months prior to surgery, Marmoset A was trained to sit in a small primate chair following methods previously described (Lu et al. 2001; Remington et al. 2012; Osmanski et al. 2013; Nummela et al. 2017). Under sterile conditions, Marmoset A was implanted with an acrylic head cap with titanium posts to stabilize the head using methods described in detail previously (Nummela et al., 2017). During the implant surgery, recording chambers were placed over premotor area A6DR and parietal area MIP based on stereotaxic coordinates (Paxinos et al., 2012). Custom 3D printed (Proto Labs) recording chambers were adhered to the skull using C&B-Metabond (Parkell, Inc.). The skull exposed within each recording chamber was covered by a thin layer of C&B-Metabond.

After recovery from head implant surgery, Marmoset A was trained to acclimate to head-restraint while sitting comfortably in a custom designed primate chair. Over several months, he was trained to perform several basic tasks including central fixation (Mitchell et. al., 2014), saccade tasks towards peripherally detected stimuli (Nummela et. al., 2017), and free viewing of natural images. After preliminary training, a second surgery was performed to create craniotomies and perform virus injections in both recording chambers according to the procedures described above. Isoflurane anesthesia was delivered with a custom 3D printed (Proto Labs) marmoset anesthesia mask rather than using endotracheal intubation. This mask was designed to fit onto the Kopf bite bar of our stereotaxic frame and formed a seal with the face using a custom cut sheet of clear, food grade silicone rubber.

Craniotomies were sealed with a thick layer of silastic gel (Kwik-Sil; World Precision Instruments) to protect the brain from infection and reduce granulation growth (Spitler & Gothard, 2008). Post-operative recovery from craniotomies required removal of silastic and flushing the craniotomy with sterile saline to remove coagulated blood until the tissue stabilized. After stabilization, the dura at each craniotomy site was excised under sterile conditions. A thin layer (<1mm) of Silastic was then applied to seal the open craniotomy, which was thin enough to enable passage of electrodes for recordings. The silastic remained in place for the duration of the study. When applied correctly, the silastic has been observed to limit the growth of granulation tissue, prevent infection (Spitler & Gothard, 2008), and can also be penetrated by linear array silicon probes with minimal risk of damage to the probes. Further, penetration sites are naturally sealed by the Silastic after removal of the electrodes.

Awake and Anaesthetized Marmoset Electrophysiology and Optogenetic Stimulation

A 64-channel silicone array (NeuroNexus, Inc.) was used to record neural signals during optogenetic stimulation while Marmoset A free-viewed natural images under head fixation [70]. Sub-millimeter depth control of the array was achieved using a custom-built X-Y stage. The stage mounted onto the recording chamber and carried a light-weight screw microdrive (Crist Instrument, 3-NRMD). The 64-channel array consisted of 2 probe shanks separated by 200 microns. Each shank consisted of 32 channels with 35 microns spacing between contacts. All arrays were 50 microns thick and had sharpened tips. For the best recording quality, arrays were electro-plated with PEDOT, a method that has been shown to increase signal/noise ratios[71,72].

To deliver light pulses for optogenetic stimulation, a guide tube was built into the X-Y stage oriented to direct a fiber optic cannula to a point on the silastic barrier immediately adjacent to the penetration point of the electrode array. An uncleaved fiber optic cannula (ThorLabs - 400um core, .39NA) was cut using an optical scribe to a length whereby the end of the probe touched the silastic without applying pressure when fully inserted into the guide tube.

In preparation for awake electrophysiology recording, Marmoset A was seated in a primate chair and head fixed. The head stage was then mounted onto the premotor chamber, the fiber optic cannula was inserted into the guide tube, and the electrodes were lowered into cortex while viewing electrophysiological signals (Open Ephys GUI). Initial array insertion into cortex followed a slow “two turns in, one turn out” procedure (each turn of the microdrive is equivalent to 250uM), which prolonged the insertion process to occur over a span of ~30 minutes. This procedure prevented silastic and cortical dimpling-related unit activity suppression and movement of units along the array during recording. All recordings were amplified and digitized at 30KHz using an Intan recording headstage. When units were apparent across all channels in the array (typically at a depth of ~1mm-1.5mm), optogenetic ChR2 stimulation experiments began. During recordings, Marmoset A free-viewed natural images while receiving periodic Ensure from a tube placed in the mouth and an automated syringe pump. Data were collected with this animal over 10 recording sessions spanning a month.

Optogenetic stimulation in awake and anaesthetized recording preparations in the marmoset was conducted using two general protocols for ChR2 stimulation and Jaws stimulation. In all cases, stimulation was delivered from a 400 um core diameter, 0.39 NA

fiberoptic cannula positioned closely over the cortical recording site, usually with a slight angle oriented towards the electrode array at depth. Laser pulses were controlled with a custom-built Arduino device capable of sending four independent TTL pulse trains from BNC connectors. In cases of simultaneous Jaws and ChR2 stimulation, two channels were dedicated to controlling laser pulses and the remaining two channels sent encoded laser metadata to the recording system. In the case of ChR2 stimulation, 20ms-50ms blue light pulses were delivered with a frequency of 5Hz. For each pulse, a jitter variable was set to randomly choose a value from 0-75ms and add or subtract this value from the otherwise periodic pulse times. For Marmoset A (**Figure 1**) and K (**Figure 6**), blue light was delivered from a 470nm LED with a measured output of 16mW (470nm, 127.3 mW/mm^2 at tip). Additional output powers were tested for mDlx-ChR2 titration: 8mW (63.6mW/mm^2) and 4mW (31.8 mW/mm^2). In mouse experiments, blue light was delivered from a 473nM solid state diode-pumped crystal laser (CrystaLaser) with output powers of 5mW (39.79mW/mm^2), 10mW (79.57mW/mm^2), 15mW (119.36mW/mm^2), or 20mW (159.15mW/mm^2). In experiments using an awake recording preparation (Marmoset A - **Figure 1**), light travelled through at least 1mm of clear silastic material, thus attenuating the light power by more than 70% of the values measured at the fiberoptic tip by geometric light falloff alone before hitting the brain surface [73,74]. In anaesthetized experiments (Marmoset K – **Figure 6**), the fiberoptic was usually 0.5 mm from the brain surface, which would attenuate intensity values by more than 50% at the brain surface [73]. In the case of Jaws stimulation, 250-750 ms light pulses were delivered with a frequency ranging from 1.5 Hz to 0.5 Hz. Similarly, a jitter value ranging from 0-200 ms was added or subtracted from otherwise rhythmic pulse times to avoid any

intrinsic entrainment of neural activity. For Marmoset K and mouse experiments, 561nM light was delivered from a solid-state diode-pumped crystal laser (CrystaLaser) with output power ranging from 5 mW to 20 mW. To test the suppression of ChR2-evoked neural activity by Jaws, the above protocols were executed simultaneously. In this configuration, neural activity induced by ChR2 events within the Jaws stimulation window was compared to ChR2 events outside of simultaneous Jaws stimulation.

Anaesthetized marmoset electrophysiological recordings were conducted with Marmoset K (**Figure 6**) six weeks after viral injection surgery. Prior to surgery, a custom electrode array armature was built out of acrylic, metal, and epoxy, which could be attached to a stereotaxic arm. This device was used for mouse recordings as well. Marmoset K was anaesthetized using isoflurane delivered through a custom marmoset anesthesia mask described above. Marmoset K was stabilized in a stereotactic frame using ear bars and a bite bar. An incision in the scalp was made and the premotor ChR2+Jaws injection craniotomy created for viral injection was re-opened. The edges of the craniotomy were expanded using a dental rotary tool, which aided in granulation tissue removal. Once the craniotomy was clear and dura was exposed, the dura was excised using a hooked syringe tip. A fiber optic cannula held by a stereotaxic arm was lowered and inserted into the small pool of saline maintained in the craniotomy. The electrode array was lowered into the brain and electrophysiological recordings with ChR2 optogenetic stimulation were conducted as described above.

To increase yields of recorded units when using isoflurane alone in preliminary anaesthetized experiments, an anesthetic protocol was developed to include, in addition to isoflurane, a dose of buprenorphine HCl (.01-.02 mg/kg) and a loading dose of

dexmedetomidine (2.5 ug) followed by a continuous drip of dexmedetomidine (5-40 ug/kg/h) [75]. This allowed an overall reduction in concomitant isoflurane delivery, resulting in increased background cortical activity and general excitability. In this case, the animal was intubated to facilitate manual pumping of breaths in the case of severe respiratory depression. Anesthesia for Marmoset K was titrated using this protocol and a stable plane was achieved using .25% isoflurane and 40ug/kg/hr of dexmedetomidine. After the animal was stabilized, ChR2 and Jaws optogenetic stimulation and electrophysiological recordings were conducted as described above. After anaesthetized recording procedures, subjects were immediately euthanized and perfused according to procedures described below.

Mouse Procedures

Injection surgeries and optogenetic electrophysiology recordings in the mouse were conducted to perform initial tests of viral expression, dilution titrations of viral solutions, and to, in general, pioneer methods to be translated to the marmoset. Injection surgeries were performed as above, but with significantly lower volumes (1x 200-400nL per anatomical area injected at one site over 3 cortical depths) and largely targeting the bilateral M1/M2 projection (Bregma +1.5mm AP, +/- 1.5mm LR), as above in the marmoset targeting of bilateral premotor cortex, areas A6 dorsal rostral and A6 dorsal caudal (A6DR/A6DC). Tests of potential spontaneous recombination in viral vectors were conducted in M1/M2 or in posterior vision areas (Bregma -2.5mm AP, +/-2mm LR). In these experiments, AAV2/retro-pmSyn1-EBFP-Cre was injected into left M1/M2 and AAV2/8-CAG-FLEx-Jaws-KGC-GFP-ER2, AAV2/8-CAG-FLEx-ChR2-tdtomato, or a 1:1 combination of the two were injected into right M1/M2. Following initial histological

injection tests of these vectors, 1:1, 1:2, 1:5, and 1:10 dilutions of these viral solutions were tested. For animals intended for awake electrophysiology procedures, injection procedures followed the implantation of a 3D-printed headframe to the skull using previously described procedures [76]. Following implantation and injection surgery, craniotomies were sealed with Silastic material as described above. Following an expression time of 1.5 weeks, animals were sacrificed for histology or used for electrophysiology experiments.

Mice that participated in awake electrophysiology experiments were acclimated to a head fixed, freely-rotating run wheel apparatus[76] during the 1.5 week expression time. After this period and prior to recording, mice were first anaesthetized using 1-2% isoflurane to open craniotomies and perform granulation tissue removal if necessary. They were immediately head fixed onto the run wheel apparatus, where they recovered from anesthesia. A stereotaxic arm-held electrode array, as described above, was lowered into cortex while recording signals using the Intan RHD2000 software. Fiber optic cannulae were placed in position directly above cortex for ChR2 and Jaws stimulation during recordings. The electrode and cannulae were moved between ChR2/Jaws and Cre injection craniotomies to test signals at axon terminal sites and the effects of terminal stimulation. At the end of a recording session, craniotomies were re-sealed with silastic. No more than 3 recording sessions were performed per animal. In the case of anaesthetized electrophysiology experiments, scalp incisions were sutured post injection surgery. Animals were anaesthetized using 1-2% isoflurane and secured into a stereotaxic device using ear bars and a bite bar. An incision was made in the scalp and tissue was cleared from injection craniotomy sites. Electrode arrays and cannulae were

put in position and isoflurane was lowered while measuring breaths per minute and monitoring for signs of arousal. Once a stable anesthetic plane was found using the lowest concentration of isoflurane (.5%-1%), stimulation protocol as described above were executed while recording electrophysiology signals.

Histology

At the termination of electrophysiology experiments or after sufficient virus expression time transpired in the mouse and marmoset, animals were transcardially perfused with 1X PBS or saline solution followed by 4% paraformaldehyde in 1X PBS or 10% formalin solution. Mouse tissue was post-fixed overnight and coronally sliced in 50um-80um sections on a vibratome prior to mounting and cover-slipping sections as necessary. Marmoset tissue was post-fixed for two days and incubated in sucrose solution until neutrally buoyant in 30% sucrose solution. Frozen coronal slices were cut to a thickness of 50um-80um on a microtome and mounted and cover-slipped as necessary or stored in 1x PBS with .05% azide. All sections were imaged using a confocal microscope (Olympus FV1000) or an automated epifluorescence slide scanner (Olympus VS110). Some fluorescent reporter signals required amplification using immunohistochemistry staining after remaining in storage for 3 months or more. Anti-RFP, anti-GFP, and anti-Cre antibodies were utilized in this study, generally in a 1:1000 concentration with 1-3 marmoset sections in a well and followed by fluorescent secondary antibodies with a 1:100 concentration. Image processing was performed using custom Matlab (2022b, Mathworks) scripts, FIJI 1.54h [77], QuPath 5.1 [78], OlyVIA 2.9 (Olympus Scientific Solutions), and Photoshop (Adobe).

Data Analysis

In addition to image visualization optimization, viral reporter expression levels were quantified using manual cell counting and automated tissue classification. Manual cell counting was performed on an epifluorescence slide scanner (Olympus VS110) images of 50um-thick marmoset tissue sections. Slide scanner images were used due to their high throughput efficiency. Custom Matlab scripts were used to first separate color channels of interest, apply a square root transformation to each image matrix, and perform levels corrections. Images were imported into Image J and manually labelled using the Cell Counter tool. Opsin positive cell bodies were identified by the characteristic hollow spheroid shape of cell membrane labelling. Slightly out of focus cell bodies were included in this counting procedure. For co-expression counting, two-channel images were imported into ImageJ and any evidence of overlapping spheroid-shaped labelling was counted as a positively co-expressing cell body regardless of differences in labelling intensity. For the AAV9 intersection experiment involving Marmoset A, the intensity and density of neuropil labeling made it impossible to perform accurate cell body counting. Therefore, QuPath was used to perform automated tissue classification using an in-built artificial network and a training procedure that provided the network with training images of examples of no tissue, un-labelled tissue, labelled tissue with healthy expression, and labelled tissue with unhealthy over-expression. One-channel images were scaled to 775px/mm, baseline subtracted, square root transformed, and intensity corrected to bring the scope of expression intensity within display range. Pre-processing in QuPath consisted of .5px gaussian smoothing to emphasize sub-cellular features and 4x gaussian smoothing to emphasize broader features. Principal components analysis feature

normalization was also performed. Training images were submitted to a 5-layer artificial neural net with a sigmoid activation function. For training image selection, the distinction between healthy and unhealthy labelled tissue was the clear and distributed presence of fluorescent puncta that likely reflect fluorescent protein aggregates and/or degenerating neural processes. Labelled healthy tissue was defined by spherically labelled cell bodies without puncta and included terminal labelling, such as labelling found in basal ganglia and claustrum. This classification procedure was summarized by dividing the area classified as healthy or unhealthy expression by the sum of areas classified as healthy, unhealthy, and un-labelled tissue. Cortex specific quantification was performed by masking out subcortical structures from the calculated percentages. Cell counts were performed using the Cell Counter function in FIJI. The VS110 slide scanner depth of field estimation for volumetric cell labelling density was performed by taking a multi-focal-plane image of labelled tissue, finding cells of interest, and moving through the stack to estimate the range by which those cells would be included in cell counting.

For data recorded from Marmoset A and K, electrophysiological data were recorded using the OpenEphys software and were spike sorted after common mode average referencing and high pass filtering (passband +300Hz) using Kilosort2. Outputs from the spike sorting algorithms were manually labeled using the 'phy' GUI (https://github/kwikteam/phy). Units were accepted if they demonstrated bi-phasic waveforms localized to adjacent channels, had PCA representations showing clear separation from noise, and demonstrated physiologically plausible inter-spike intervals. For data recorded from Marmoset Y and from mice, electrophysiological data were recorded using the Intan RHD2000 recording interface and preprocessed using common

mode averaging and bandpass filtering (800-1600Hz). Custom Matlab scripts identified spikes via user defined amplitude and inter-spike interval criteria for each recording channel. Identified spike waveforms were visualized and channels were rejected if dominated by non-physiological waveforms. Spikes identified using this method were not necessarily well isolated and reflect multi-unit activity present on each recording channel. Local field potentials (LFPs) were calculated for each channel by performing common mode referencing, lowpass filtering (passband -300Hz), and filtering out 60Hz line noise.

Laser-triggered optogenetic activity was summarized for each sorted unit or recording channel via raster plots and mean firing activity calculated in 1ms bins from a sliding gaussian window (3ms for shorter ChR2 stimulation pulses and 15ms for longer Jaws stimulation pulses). The optogenetic modulation index was calculated at each millisecond bin for each unit by the difference of laser modulated firing rate from a mean baseline firing rate divided by the sum of laser modulated firing rate and mean baseline firing rate. The mean baseline firing rate was calculated using a window of -20 to -5 milliseconds prior to laser onset.

ACKNOWLEDGMENTS

This work is supported by Del Monte Institute for Neuroscience, Schmitt Program on Integrative Neuroscience, and the National Institutes of Health (P50HD103536 to KHW, 5R01EY030998-05 to JFM). We thank members of Mitchell lab, especially Dina Graf, for technical assistance and also members of Wang lab for thoughtful discussions and technical assistance.

CONFLICT OF INTEREST

The authors declare no competing financial interests.

DECLARATION OF GENERATIVE AI AND AI-ASSISTED TECHNOLOGIES IN THE WRITING PROCESS

The authors declare no use of generative AI or large language models in the production of this manuscript.

REFERENCES

1. Deisseroth, K. (2014). Circuit dynamics of adaptive and maladaptive behaviour. Nature *505*, 309-317. 10.1038/nature12982.
2. Boyden, E.S., Zhang, F., Bamberg, E., Nagel, G., and Deisseroth, K. (2005). Millisecond-timescale, genetically targeted optical control of neural activity. Nat Neurosci *8*, 1263-1268. 10.1038/nn1525.
3. El-Shamayleh, Y., and Horwitz, G.D. (2019). Primate optogenetics: Progress and prognosis. Proc Natl Acad Sci U S A *116*, 26195-26203. 10.1073/pnas.1902284116.
4. Tremblay, S., Acker, L., Afraz, A., Albaugh, D.L., Amita, H., Andrei, A.R., Angelucci, A., Aschner, A., Balan, P.F., Basso, M.A., et al. (2020). An Open Resource for Non-human Primate Optogenetics. Neuron *108*, 1075-1090 e1076. 10.1016/j.neuron.2020.09.027.
5. Goldman-Rakic, P.S., and Rakic, P. (1991). Preface: Cerebral Cortex Has Come of Age. Cerebral Cortex *1*, 1-1. 10.1093/cercor/1.1.1.
6. Magrou, L., Joyce, M.K.P., Froudist-Walsh, S., Datta, D., Wang, X.J., Martinez-Trujillo, J., and Arnsten, A.F.T. (2024). The meso-connectomes of mouse, marmoset, and macaque: network organization and the emergence of higher cognition. Cereb Cortex *34*. 10.1093/cercor/bhae174.
7. Bakken, T.E., Jorstad, N.L., Hu, Q., Lake, B.B., Tian, W., Kalmbach, B.E., Crow, M., Hodge, R.D., Krienen, F.M., Sorensen, S.A., et al. (2021). Comparative cellular analysis of motor cortex in human, marmoset and mouse. Nature *598*, 111-119. 10.1038/s41586-021-03465-8.
8. Horvat, S., Gamanut, R., Ercsey-Ravasz, M., Magrou, L., Gamanut, B., Van Essen, D.C., Burkhalter, A., Knoblauch, K., Toroczkai, Z., and Kennedy, H. (2016). Spatial Embedding and Wiring Cost Constrain the Functional Layout of the Cortical Network of Rodents and Primates. PLoS Biol *14*, e1002512. 10.1371/journal.pbio.1002512.
9. Niell, C.M., and Scanziani, M. (2021). How Cortical Circuits Implement Cortical Computations: Mouse Visual Cortex as a Model. Annu Rev Neurosci *44*, 517-546. 10.1146/annurev-neuro-102320-085825.
10. Miller, C.T., Freiwald, W.A., Leopold, D.A., Mitchell, J.F., Silva, A.C., and Wang, X. (2016). Marmosets: A Neuroscientific Model of Human Social Behavior. Neuron *90*, 219-233. 10.1016/j.neuron.2016.03.018.
11. Okano, H. (2021). Current Status of and Perspectives on the Application of Marmosets in Neurobiology. Annu Rev Neurosci *44*, 27-48. 10.1146/annurev-neuro-030520-101844.
12. Bakola, S., Burman, K.J., and Rosa, M.G. (2015). The cortical motor system of the marmoset monkey (Callithrix jacchus). Neurosci Res *93*, 72-81. 10.1016/j.neures.2014.11.003.
13. D'Souza, J.F., Price, N.S.C., and Hagan, M.A. (2021). Marmosets: a promising model for probing the neural mechanisms underlying complex visual networks such as the frontal-parietal network. Brain Struct Funct *226*, 3007-3022. 10.1007/s00429-021-02367-9.

14. Mitchell, J.F., and Leopold, D.A. (2015). The marmoset monkey as a model for visual neuroscience. Neuroscience Research *93*, 20-46. 10.1016/j.neures.2015.01.008.
15. Schiel, N., and Souto, A. (2017). The common marmoset: An overview of its natural history, ecology and behavior. Developmental Neurobiology.
16. Walker, J., MacLean, J., and Hatsopoulos, N.G. (2017). The marmoset as a model system for studying voluntary motor control. Developmental Neurobiology.
17. Luo, L., Callaway, E.M., and Svoboda, K. (2018). Genetic Dissection of Neural Circuits: A Decade of Progress. Neuron *98*, 256-281. 10.1016/j.neuron.2018.03.040.
18. Rajasethupathy, P., Ferenczi, E., and Deisseroth, K. (2016). Targeting Neural Circuits. Cell *165*, 524-534. 10.1016/j.cell.2016.03.047.
19. Campos, L.J., Arokiaraj, C.M., Chuapoco, M.R., Chen, X., Goeden, N., Gradinaru, V., and Fox, A.S. (2023). Advances in AAV technology for delivering genetically encoded cargo to the nonhuman primate nervous system. Curr Res Neurobiol *4*, 100086. 10.1016/j.crneur.2023.100086.
20. El-Shamayleh, Y., Ni, A.M., and Horwitz, G.D. (2016). Strategies for targeting primate neural circuits with viral vectors. J Neurophysiol *116*, 122-134. 10.1152/jn.00087.2016.
21. MacDougall, M., Nummela, S.U., Coop, S., Disney, A., Mitchell, J.F., and Miller, C.T. (2016). Optogenetic manipulation of neural circuits in awake marmosets. J Neurophysiol *116*, 1286-1294. 10.1152/jn.00197.2016.
22. Watakabe, A., Ohtsuka, M., Kinoshita, M., Takaji, M., Isa, K., Mizukami, H., Ozawa, K., Isa, T., and Yamamori, T. (2015). Comparative analyses of adeno-associated viral vector serotypes 1, 2, 5, 8 and 9 in marmoset, mouse and macaque cerebral cortex. Neurosci Res *93*, 144-157. 10.1016/j.neures.2014.09.002.
23. Ohayon, S., Grimaldi, P., Schweers, N., and Tsao, D.Y. (2013). Saccade modulation by optical and electrical stimulation in the macaque frontal eye field. J Neurosci *33*, 16684-16697. 10.1523/JNEUROSCI.2675-13.2013.
24. Dimidschstein, J., Chen, Q., Tremblay, R., Rogers, S.L., Saldi, G.A., Guo, L., Xu, Q., Liu, R., Lu, C., Chu, J., et al. (2016). A viral strategy for targeting and manipulating interneurons across vertebrate species. Nat Neurosci *19*, 1743-1749. 10.1038/nn.4430.
25. De, A., El-Shamayleh, Y., and Horwitz, G.D. (2020). Fast and reversible neural inactivation in macaque cortex by optogenetic stimulation of GABAergic neurons. Elife *9*. 10.7554/eLife.52658.
26. Fetsch, C.R., Odean, N.N., Jeurissen, D., El-Shamayleh, Y., Horwitz, G.D., and Shadlen, M.N. (2018). Focal optogenetic suppression in macaque area MT biases direction discrimination and decision confidence, but only transiently. Elife *7*. 10.7554/eLife.36523.
27. Jeurissen, D., Shushruth, S., El-Shamayleh, Y., Horwitz, G.D., and Shadlen, M.N. (2022). Deficits in decision-making induced by parietal cortex inactivation are compensated at two timescales. Neuron *110*, 1924-1931 e1925. 10.1016/j.neuron.2022.03.022.

28. Caputi, A., Melzer, S., Michael, M., and Monyer, H. (2013). The long and short of GABAergic neurons. Curr Opin Neurobiol *23*, 179-186. 10.1016/j.conb.2013.01.021.
29. Melzer, S., and Monyer, H. (2020). Diversity and function of corticopetal and corticofugal GABAergic projection neurons. Nat Rev Neurosci *21*, 499-515. 10.1038/s41583-020-0344-9.
30. Liu, Y., Latremoliere, A., Li, X., Zhang, Z., Chen, M., Wang, X., Fang, C., Zhu, J., Alexandre, C., Gao, Z., et al. (2018). Touch and tactile neuropathic pain sensitivity are set by corticospinal projections. Nature *561*, 547-550. 10.1038/s41586-018-0515-2.
31. Wang, X., Liu, Y., Li, X., Zhang, Z., Yang, H., Zhang, Y., Williams, P.R., Alwahab, N.S.A., Kapur, K., Yu, B., et al. (2017). Deconstruction of Corticospinal Circuits for Goal-Directed Motor Skills. Cell *171*, 440-455 e414. 10.1016/j.cell.2017.08.014.
32. Zhang, Z., Su, J., Tang, J., Chung, L., Page, J.C., Winter, C.C., Liu, Y., Kegeles, E., Conti, S., Zhang, Y., et al. (2024). Spinal projecting neurons in rostral ventromedial medulla co-regulate motor and sympathetic tone. Cell *187*, 3427-3444 e3421. 10.1016/j.cell.2024.04.022.
33. Cushnie, A.K., El-Nahal, H.G., Bohlen, M.O., May, P.J., Basso, M.A., Grimaldi, P., Wang, M.Z., de Velasco Ezequiel, M.F., Sommer, M.A., and Heilbronner, S.R. (2020). Using rAAV2-retro in rhesus macaques: Promise and caveats for circuit manipulation. J Neurosci Methods *345*, 108859. 10.1016/j.jneumeth.2020.108859.
34. Tervo, D.G., Hwang, B.Y., Viswanathan, S., Gaj, T., Lavzin, M., Ritola, K.D., Lindo, S., Michael, S., Kuleshova, E., Ojala, D., et al. (2016). A Designer AAV Variant Permits Efficient Retrograde Access to Projection Neurons. Neuron *92*, 372-382. 10.1016/j.neuron.2016.09.021.
35. Aschauer, D.F., Kreuz, S., and Rumpel, S. (2013). Analysis of transduction efficiency, tropism and axonal transport of AAV serotypes 1, 2, 5, 6, 8 and 9 in the mouse brain. PLoS One *8*, e76310. 10.1371/journal.pone.0076310.
36. Castle, M.J., Gershenson, Z.T., Giles, A.R., Holzbaur, E.L., and Wolfe, J.H. (2014). Adeno-associated virus serotypes 1, 8, and 9 share conserved mechanisms for anterograde and retrograde axonal transport. Hum Gene Ther *25*, 705-720. 10.1089/hum.2013.189.
37. Watakabe, A., Skibbe, H., Nakae, K., Abe, H., Ichinohe, N., Rachmadi, M.F., Wang, J., Takaji, M., Mizukami, H., Woodward, A., et al. (2023). Local and long-distance organization of prefrontal cortex circuits in the marmoset brain. Neuron *111*, 2258-2273 e2210. 10.1016/j.neuron.2023.04.028.
38. Herzog, R.W. (2007). Immune responses to AAV capsid: are mice not humans after all? Mol Ther *15*, 649-650. 10.1038/sj.mt.6300123.
39. Meyer, N.L., and Chapman, M.S. (2022). Adeno-associated virus (AAV) cell entry: structural insights. Trends Microbiol *30*, 432-451. 10.1016/j.tim.2021.09.005.
40. Chuong, A.S., Miri, M.L., Busskamp, V., Matthews, G.A., Acker, L.C., Sorensen, A.T., Young, A., Klapoetke, N.C., Henninger, M.A., Kodandaramaiah, S.B., et al.

(2014). Noninvasive optical inhibition with a red-shifted microbial rhodopsin. Nat Neurosci *17*, 1123-1129. 10.1038/nn.3752.
41. Mitchell, J.F., Sundberg, K.A., and Reynolds, J.H. (2007). Differential attention-dependent response modulation across cell classes in macaque visual area V4. Neuron *55*, 131-141. 10.1016/j.neuron.2007.06.018.
42. Becchetti, A., Gullo, F., Bruno, G., Dossi, E., Lecchi, M., and Wanke, E. (2012). Exact distinction of excitatory and inhibitory neurons in neural networks: a study with GFP-GAD67 neurons optically and electrophysiologically recognized on multielectrode arrays. Front Neural Circuits *6*, 63. 10.3389/fncir.2012.00063.
43. Nurminen, L., Merlin, S., Bijanzadeh, M., Federer, F., and Angelucci, A. (2018). Top-down feedback controls spatial summation and response amplitude in primate visual cortex. Nat Commun *9*, 2281. 10.1038/s41467-018-04500-5.
44. Hori, Y., Cléry, J.C., Schaeffer, D.J., Menon, R.S., and Everling, S. (2021). Functional Organization of Frontoparietal Cortex in the Marmoset Investigated with Awake Resting-State fMRI. Cerebral Cortex. 10.1093/cercor/bhab328.
45. Castle, M.J., Perlson, E., Holzbaur, E.L., and Wolfe, J.H. (2014). Long-distance axonal transport of AAV9 is driven by dynein and kinesin-2 and is trafficked in a highly motile Rab7-positive compartment. Mol Ther *22*, 554-566. 10.1038/mt.2013.237.
46. Dermon, C.R., and Barbas, H. (1994). Contralateral Thalamic Projections Predominantly Reach Transitional Cortices in the Rhesus Monkey. The Journal of Comparative Neurology *344*, 508-531. 10.1002/cne.903440403.
47. Carretta, D., Sbriccoli, A., Santarelli, M., Pinto, F., Granato, A., and Minciacchi, D. (1996). Crossed thalamo-cortical and cortico-thalamic projections in adult mice. Neurosci Lett *204*, 69-72. 10.1016/0304-3940(96)12319-3.
48. Alloway, K.D., Olson, M.L., and Smith, J.B. (2008). Contralateral corticothalamic projections from MI whisker cortex: potential route for modulating hemispheric interactions. J Comp Neurol *510*, 100-116. 10.1002/cne.21782.
49. Challis, R.C., Ravindra Kumar, S., Chen, X., Goertsen, D., Coughlin, G.M., Hori, A.M., Chuapoco, M.R., Otis, T.S., Miles, T.F., and Gradinaru, V. (2022). Adeno-Associated Virus Toolkit to Target Diverse Brain Cells. Annu Rev Neurosci *45*, 447-469. 10.1146/annurev-neuro-111020-100834.
50. Li, N., Chen, S., Guo, Z.V., Chen, H., Huo, Y., Inagaki, H.K., Chen, G., Davis, C., Hansel, D., Guo, C., and Svoboda, K. (2019). Spatiotemporal constraints on optogenetic inactivation in cortical circuits. Elife *8*. 10.7554/eLife.48622.
51. Zingg, B., Peng, B., Huang, J., Tao, H.W., and Zhang, L.I. (2020). Synaptic Specificity and Application of Anterograde Transsynaptic AAV for Probing Neural Circuitry. J Neurosci *40*, 3250-3267. 10.1523/JNEUROSCI.2158-19.2020.
52. Shemesh, O.A., Tanese, D., Zampini, V., Linghu, C., Piatkevich, K., Ronzitti, E., Papagiakoumou, E., Boyden, E.S., and Emiliani, V. (2017). Temporally precise single-cell-resolution optogenetics. Nat Neurosci *20*, 1796-1806. 10.1038/s41593-017-0018-8.
53. Papagiakoumou, E., Anselmi, F., Bègue, A., de Sars, V., Glückstad, J., Isacoff, E.Y., and Emiliani, V. (2010). Scanless two-photon excitation of channelrhodopsin-2. Nat Methods *7*, 848-854. 10.1038/nmeth.1505.

54. Kimura, T., Ferran, B., Tsukahara, Y., Shang, Q., Desai, S., Fedoce, A., Pimentel, D.R., Luptak, I., Adachi, T., Ido, Y., et al. (2019). Production of adeno-associated virus vectors for in vitro and in vivo applications. Sci Rep *9*, 13601. 10.1038/s41598-019-49624-w.
55. Ose, T., Autio, J.A., Ohno, M., Frey, S., Uematsu, A., Kawasaki, A., Takeda, C., Hori, Y., Nishigori, K., Nakako, T., et al. (2022). Anatomical variability, multi-modal coordinate systems, and precision targeting in the marmoset brain. NeuroImage *250*, 118965. 10.1016/j.neuroimage.2022.118965.
56. Hofherr, A., Fakler, B., and Klöcker, N. (2005). Selective Golgi export of Kir2.1 controls the stoichiometry of functional Kir2.x channel heteromers. J Cell Sci *118*, 1935-1943. 10.1242/jcs.02322.
57. Ma, D., Zerangue, N., Lin, Y.F., Collins, A., Yu, M., Jan, Y.N., and Jan, L.Y. (2001). Role of ER export signals in controlling surface potassium channel numbers. Science *291*, 316-319. 10.1126/science.291.5502.316.
58. Zingg, B., Chou, X.L., Zhang, Z.G., Mesik, L., Liang, F., Tao, H.W., and Zhang, L.I. (2017). AAV-Mediated Anterograde Transsynaptic Tagging: Mapping Corticocollicular Input-Defined Neural Pathways for Defense Behaviors. Neuron *93*, 33-47. 10.1016/j.neuron.2016.11.045.
59. Dinopoulos, A. (1994). Reciprocal Connections of the Motor Neocortical Area with the Contralateral Thalamus in the Hedgehog (Erinaceus europaeus) Brain. European Journal of Neuroscience *6*, 374-380. https://doi.org/10.1111/j.1460-9568.1994.tb00280.x.
60. Huer, J., Saxena, P., and Treue, S. (2024). Pathway-selective optogenetics reveals the functional anatomy of top-down attentional modulation in the macaque visual cortex. Proc Natl Acad Sci U S A *121*, e2304511121. 10.1073/pnas.2304511121.
61. Andrei, A.R., and Dragoi, V. (2025). Optogenetic modulation of long-range cortical circuits in awake nonhuman primates. Nat Protoc. 10.1038/s41596-024-01123-7.
62. Wietek, J., Nozownik, A., Pulin, M., Saraf-Sinik, I., Matosevich, N., Gowrishankar, R., Gat, A., Malan, D., Brown, B.J., Dine, J., et al. (2024). A bistable inhibitory optoGPCR for multiplexed optogenetic control of neural circuits. Nat Methods *21*, 1275-1287. 10.1038/s41592-024-02285-8.
63. Katz, L.N., Bohlen, M.O., Yu, G., Mejias-Aponte, C., Sommer, M.A., and Krauzlis, R.J. (2025). Optogenetic Manipulation of Covert Attention in the Nonhuman Primate. J Cogn Neurosci *37*, 266-285. 10.1162/jocn_a_02274.
64. Watanabe, H., Sano, H., Chiken, S., Kobayashi, K., Fukata, Y., Fukata, M., Mushiake, H., and Nambu, A. (2020). Forelimb movements evoked by optogenetic stimulation of the macaque motor cortex. Nat Commun *11*, 3253. 10.1038/s41467-020-16883-5.
65. Ebina, T., Obara, K., Watakabe, A., Masamizu, Y., Terada, S.I., Matoba, R., Takaji, M., Hatanaka, N., Nambu, A., Mizukami, H., et al. (2019). Arm movements induced by noninvasive optogenetic stimulation of the motor cortex in the common marmoset. Proc Natl Acad Sci U S A *116*, 22844-22850. 10.1073/pnas.1903445116.

66. Maeda, K., Inoue, K.I., Takada, M., and Hikosaka, O. (2023). Environmental context-dependent activation of dopamine neurons via putative amygdala-nigra pathway in macaques. Nat Commun *14*, 2282. 10.1038/s41467-023-37584-9.
67. Vierock, J., Rodriguez-Rozada, S., Dieter, A., Pieper, F., Sims, R., Tenedini, F., Bergs, A.C.F., Bendifallah, I., Zhou, F., Zeitzschel, N., et al. (2021). BiPOLES is an optogenetic tool developed for bidirectional dual-color control of neurons. Nat Commun *12*, 4527. 10.1038/s41467-021-24759-5.
68. Inoue, K.I., Takada, M., and Matsumoto, M. (2015). Neuronal and behavioural modulations by pathway-selective optogenetic stimulation of the primate oculomotor system. Nat Commun *6*, 8378. 10.1038/ncomms9378.
69. Cavanaugh, J., Monosov, I.E., McAlonan, K., Berman, R., Smith, M.K., Cao, V., Wang, K.H., Boyden, E.S., and Wurtz, R.H. (2012). Optogenetic inactivation modifies monkey visuomotor behavior. Neuron *76*, 901-907. 10.1016/j.neuron.2012.10.016.
70. Bucklaew, A., Coop, S.H., and Mitchell, J.F. (2023). Electrophysiology of Laminar Cortical Activity in the Common Marmoset. JoVE, e65397. doi:10.3791/65397.
71. Ludwig, K.A., Uram, J.D., Yang, J., Martin, D.C., and Kipke, D.R. (2006). Chronic neural recordings using silicon microelectrode arrays electrochemically deposited with a poly(3,4-ethylenedioxythiophene) (PEDOT) film. J Neural Eng *3*, 59-70. 10.1088/1741-2560/3/1/007.
72. Ludwig, K.A., Langhals, N.B., Joseph, M.D., Richardson-Burns, S.M., Hendricks, J.L., and Kipke, D.R. (2011). Poly(3,4-ethylenedioxythiophene) (PEDOT) polymer coatings facilitate smaller neural recording electrodes. J Neural Eng *8*, 014001. 10.1088/1741-2560/8/1/014001.
73. Yizhar, O., Fenno, L.E., Davidson, T.J., Mogri, M., and Deisseroth, K. (2011). Optogenetics in neural systems. Neuron *71*, 9-34. 10.1016/j.neuron.2011.06.004.
74. Deisseroth, K. Predicted irradiance values: model based on direct measurements in mammalian brain tissue. https://web.stanford.edu/group/dlab/cgi-bin/graph/chart.php.
75. Muta, K., Hata, J., Kawaguchi, N., Haga, Y., Yoshimaru, D., Hagiya, K., Kaneko, T., Miyabe-Nishiwaki, T., Komaki, Y., Seki, F., et al. (2023). Effect of sedatives or anesthetics on the measurement of resting brain function in common marmosets. Cereb Cortex *33*, 5148-5162. 10.1093/cercor/bhac406.
76. Chockanathan, U., Warner, E.J., Turpin, L., O'Banion, M.K., and Padmanabhan, K. (2020). Altered dorsal CA1 neuronal population coding in the APP/PS1 mouse model of Alzheimer's disease. Sci Rep *10*, 1077. 10.1038/s41598-020-58038-y.
77. Schindelin, J., Arganda-Carreras, I., Frise, E., Kaynig, V., Longair, M., Pietzsch, T., Preibisch, S., Rueden, C., Saalfeld, S., Schmid, B., et al. (2012). Fiji: an open-source platform for biological-image analysis. Nat Methods *9*, 676-682. 10.1038/nmeth.2019.
78. Bankhead, P., Loughrey, M.B., Fernandez, J.A., Dombrowski, Y., McArt, D.G., Dunne, P.D., McQuaid, S., Gray, R.T., Murray, L.J., Coleman, H.G., et al. (2017). QuPath: Open source software for digital pathology image analysis. Sci Rep *7*, 16878. 10.1038/s41598-017-17204-5.

FIGURES

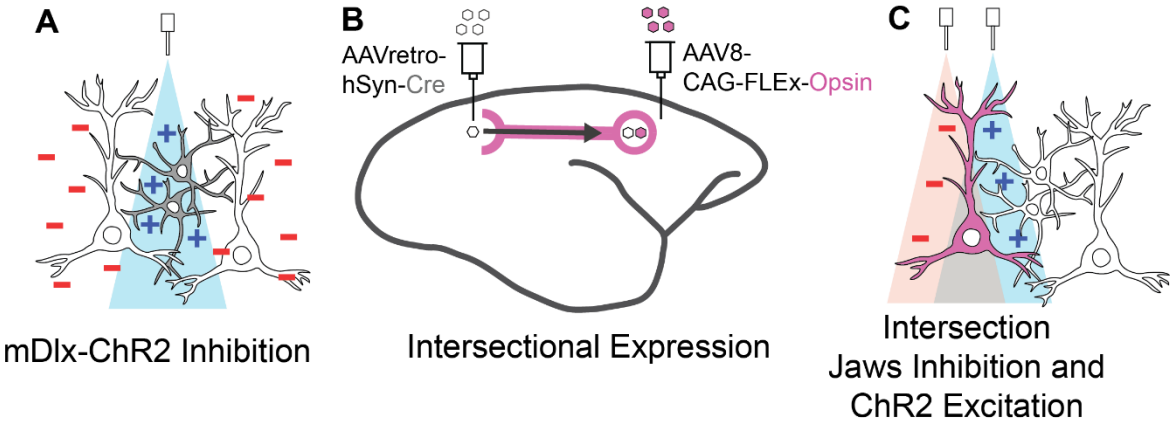

Graphical Abstract

Graphical Abstract

A: Local suppression of cortical activity that is non-selective across cell classes can be accomplished by excitation of inhibitory interneurons expressing mDlx-ChR2 yielding broad inhibition. **B:** By contrast, targeting a specific cortico-cortical projection pathway for suppression can be accomplished through an intersectional approach. For a successful intersection, a retrograde AAV carrying hSyn-Cre is injected at the projection terminal and a locally expressing AAV carrying CAG-FLEx-opsin is injected at the soma. These viruses meet at the nucleus and yield opsin expression restricted to projection neurons. **C:** Inhibition or excitation is possible in targeted projection neurons due to co-expression of the blue light triggered excitatory opsin ChR2 or the red shifted inhibitory opsin Jaws.

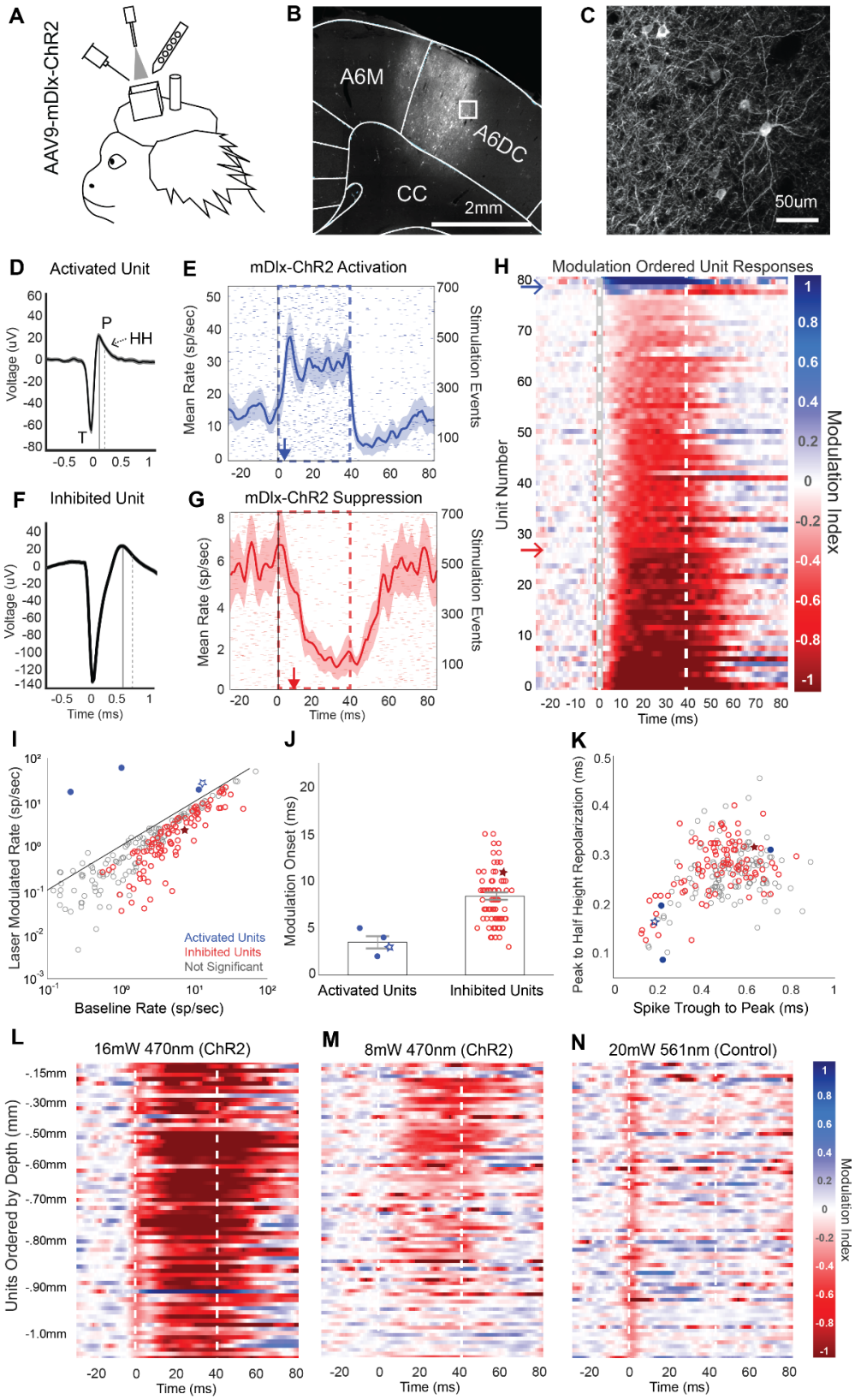

Figure 1. AAV9-mDlx-ChR2-mediated Local Cortical Inhibition in the Marmoset

Figure 1. AAV9-mDlx-ChR2-mediated Local Cortical Inhibition in the Marmoset

A Electrophysiology during optical stimulation was conducted in an awake, head fixed marmoset. 1.5uL of AAV9-mDlx-ChR2 was injected at two sites within a craniotomy over premotor area A6DC 8 months prior to optogenetic experiments. **B-C** Histology of mDlx-ChR2+ positive inhibitory interneurons. **D** Average spike waveform of an excited unit. T indicates the trough of the spike. P indicates the post-depolarization voltage peak, marked in time by the solid line. HH indicates the half height of the repolarization voltage curve, which is marked in time by the dashed line. This unit is displayed as a red star in panels I-J. **E** Laser triggered PSTH of the unit in D. The red arrow indicates the modulation onset time. Shaded regions indicate 2 standard error of the mean (SEM). **F** Average spike waveform of an example suppressed unit. The solid and dashed lines indicate the peak and repolarization half height, as previous. This unit is displayed as a blue star in panels I-J. **G** Light triggered PSTH of the unit in F. The blue arrow indicates the modulation onset time. **H** Spike sorted units ordered by degree of laser-stimulated firing modulation. Red indicates excitation. Blue indicates suppression. Dotted lines indicate laser duration. Modulation index calculation is detailed in Methods. **I** The laser triggered firing rate of units plotted against their baseline firing rate. Red points are significantly activated units relative to baseline. Blue points are suppressed. **J** Excited and inhibited units are plotted by the onset of laser-triggered modulation. Onset was estimated by the first timepoint at which the laser modulation firing rate rises above or drops below baseline +/- 2 SEM. **K** Spike waveforms were characterized using trough (T) to peak (P) duration and peak (P) to repolarization half height (HH) duration. **L-N** Blue laser (470nm) power was reduced to test modulation of laser-triggered optogenetic effect in a continuous recording. Green light (561nm) at a high power was used as a control to show no neural suppression by laser heat. Units are ordered by cortical depth.

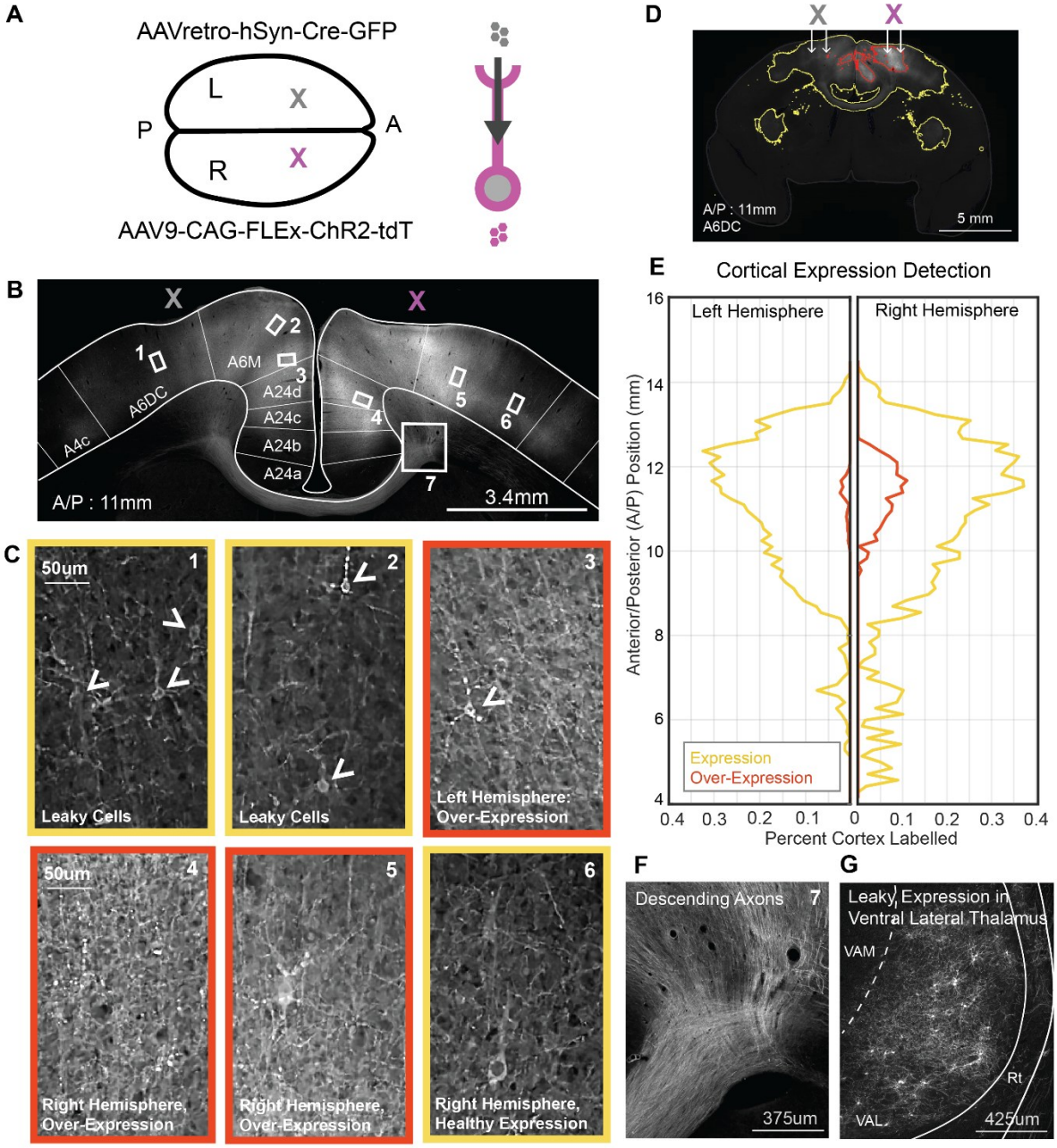

Figure 2. AAV9-based Intersectional Strategy Yields Efficient but Leaky Cross-Callosal ChR2 Expression

Figure 2. AAV9-based Intersectional Strategy Yields Efficient but Leaky Cross-Callosal ChR2 Expression

A Intersection viruses were delivered to left (Cre-gray) and right (ChR2-magenta) A6DC in marmoset premotor cortex. **B** Example premotor cortex at expression peak. **C** Zoom-ins numbered accordingly. Border color indicates expression classification as in panel E. Blebbing puncta are indications of over-expression. Arrows indicate leaky soma labelling in left cortex. **D** Example section after automated tissue classification. Red indicates over-expression. Yellow indicates typical expression. Despite subcortical labeling in basal ganglia and claustrum, only cortex was included in quantification. **E** Percent cortical area covered by healthy and unhealthy classification in imaged coronal sections. Subcortical labelling was excluded. **F** Labelled descending and decussating axons. **G** Leaky soma labelling in a motor-related area of thalamus, Ventral Anterior Lateral Thalamus (VAL). VAM Ventral Anterior Medial Thalamus. Rt Reticular nucleus.

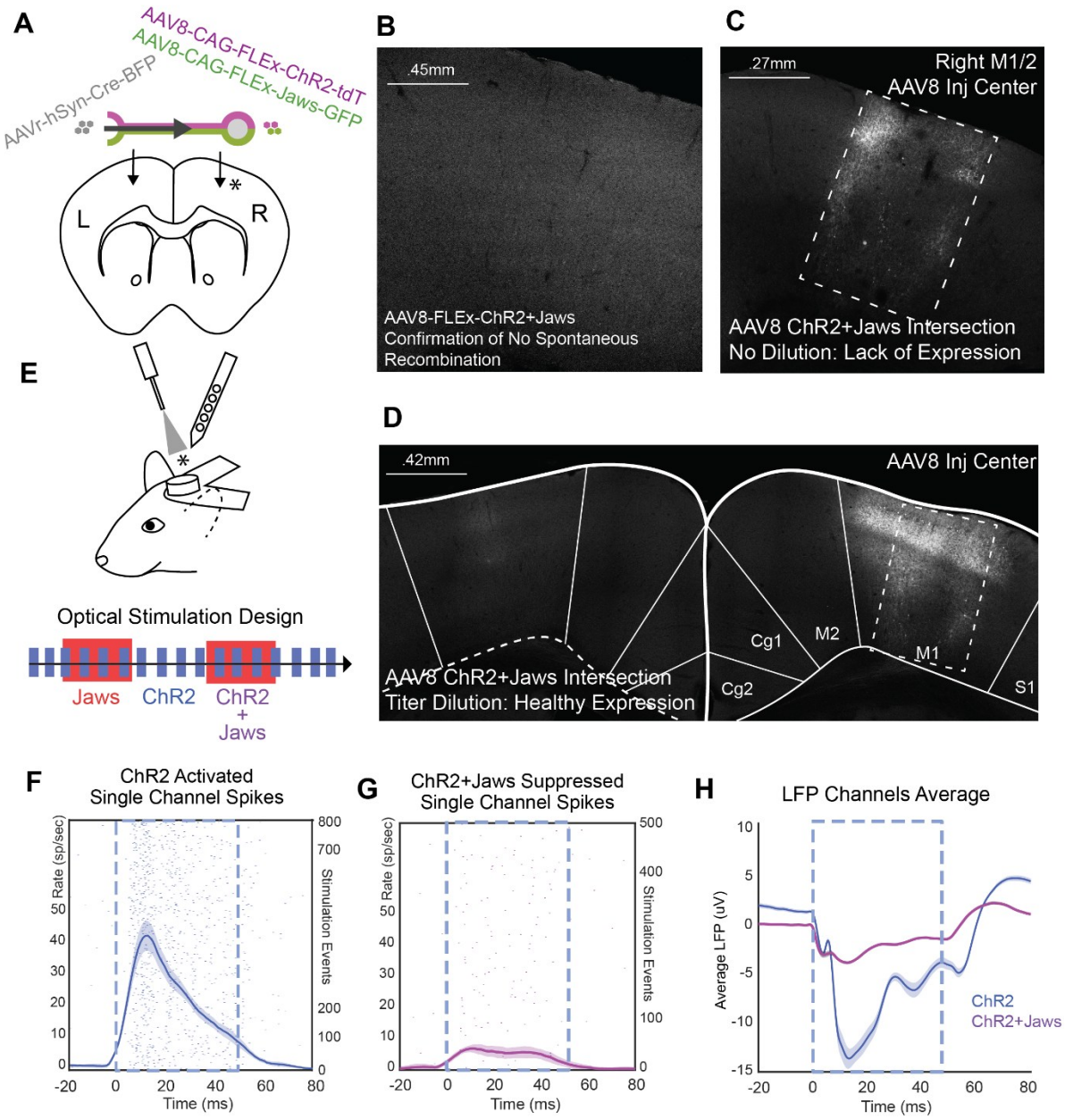

Figure 3. Evaluation and Titration of AAV8-Based Intersectional Jaws and ChR2 Expression in the Mouse Brain

Figure 3. Evaluation and Titration of AAV8-Based Intersectional Jaws and ChR2 Expression in the Mouse Brain

A Cross-callosal intersection strategy using a 1:1 mixture of ChR2 and Jaws virus. Asterisk indicates electrophysiology recording site. **B** AAV8-flex-ChR2+Jaws confirms no expression in absence of Cre. **C** Undiluted injection showed lack of expression in the area surrounding the injection site (dashed box) not explainable by tissue damage caused by the injection pipette. **D** AAVretro-Cre (left) and AAV8-ChR2+AAV8-Jaws (right) injection sites of 1:2 diluted viral solution showing healthy expression in the area surrounding the AAV8 injection site (dashed box). Axon terminals are evident in the left hemisphere. **E** Head fixed awake mouse optical stimulation strategy. ChR2 stimulation pulses were delivered in the presence and absence of long duration Jaws stimulation pulses. **F** ChR2 laser triggered raster and PSTH of multi-unit activity from a channel showing excitation. **G** ChR2 laser triggered raster and PSTH during Jaws stimulation showing suppression. **H** Mean local field potential of ChR2 and ChR2+Jaws stimulation showing the population activation response to ChR2 stimulation and the inhibition of that effect with simultaneous stimulation of Jaws.

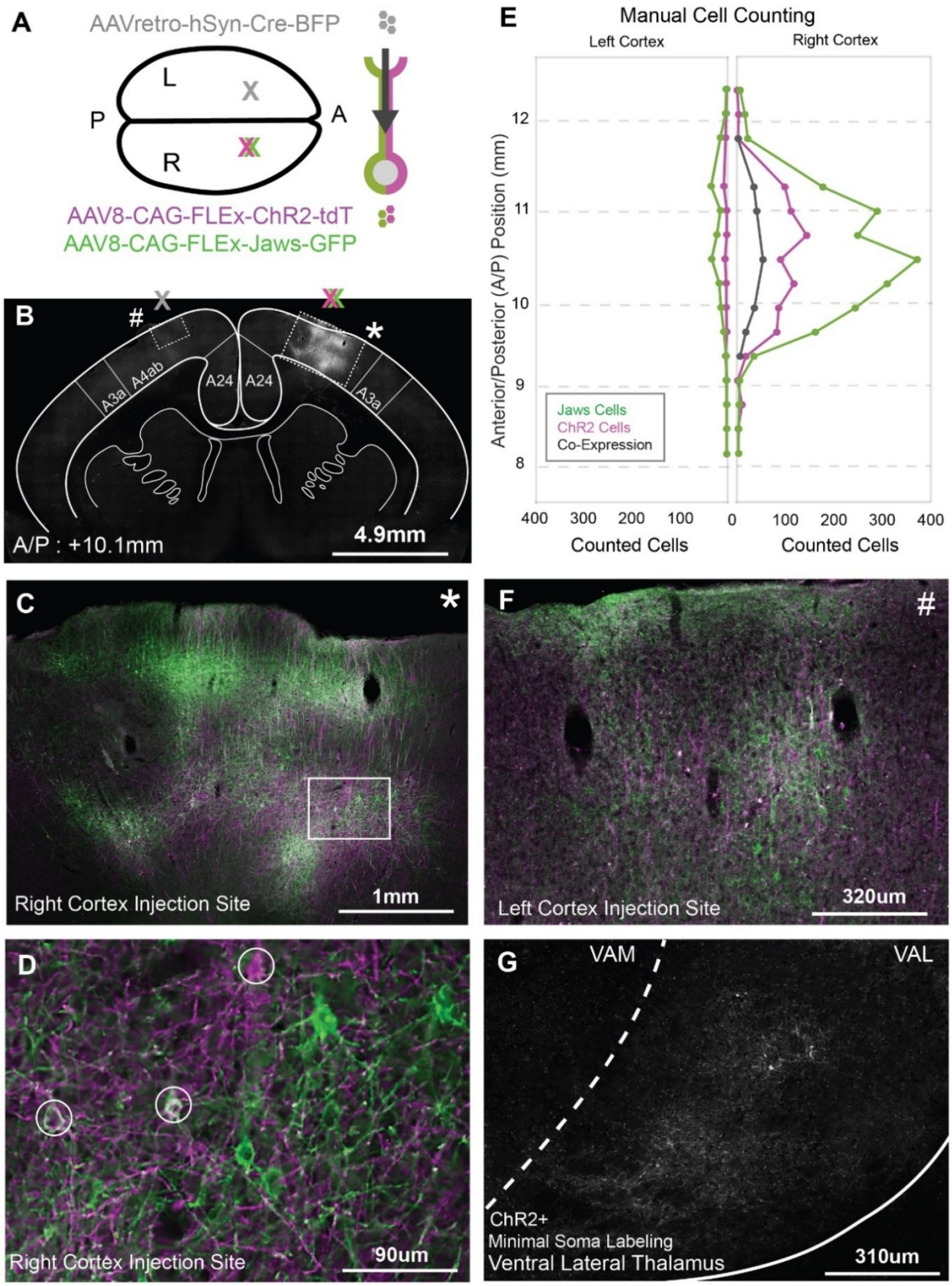

Figure 4. Efficient and Specific Cross-Callosal Intersectional Expression of ChR2 and Jaws using AAV8

Figure 4. Efficient and Specific Cross-Callosal Intersectional Expression of ChR2 and Jaws using AAV8

A-B Intersection viruses were delivered to left (Cre) and right (ChR2+Jaws) A6DC/A4ab in marmoset cortex. Squares indicate zoom-ins for panels C and F. **C** Zoom in of the AAV8-ChR2+Jaws injection site showing superficial and deep cortical layer expression. **D** Further zoom in from Panel C showing healthy soma and dendrite labelling. Circles indicate co-expression of Jaws (green) and ChR2 (magenta). **E** Manual cell soma counting quantification. Each circle indicates the quantity of counted, labelled soma from an individual coronal section. **F** Zoom in of the Cre injection site showing axon expression and some leaky soma labeling. **G** Labelling in motor thalamus (Ventral Anterior Lateral thalamus (VAL)) consists of axons and minimal leaky soma, in contrast to the expression found in the AAV9 condition.

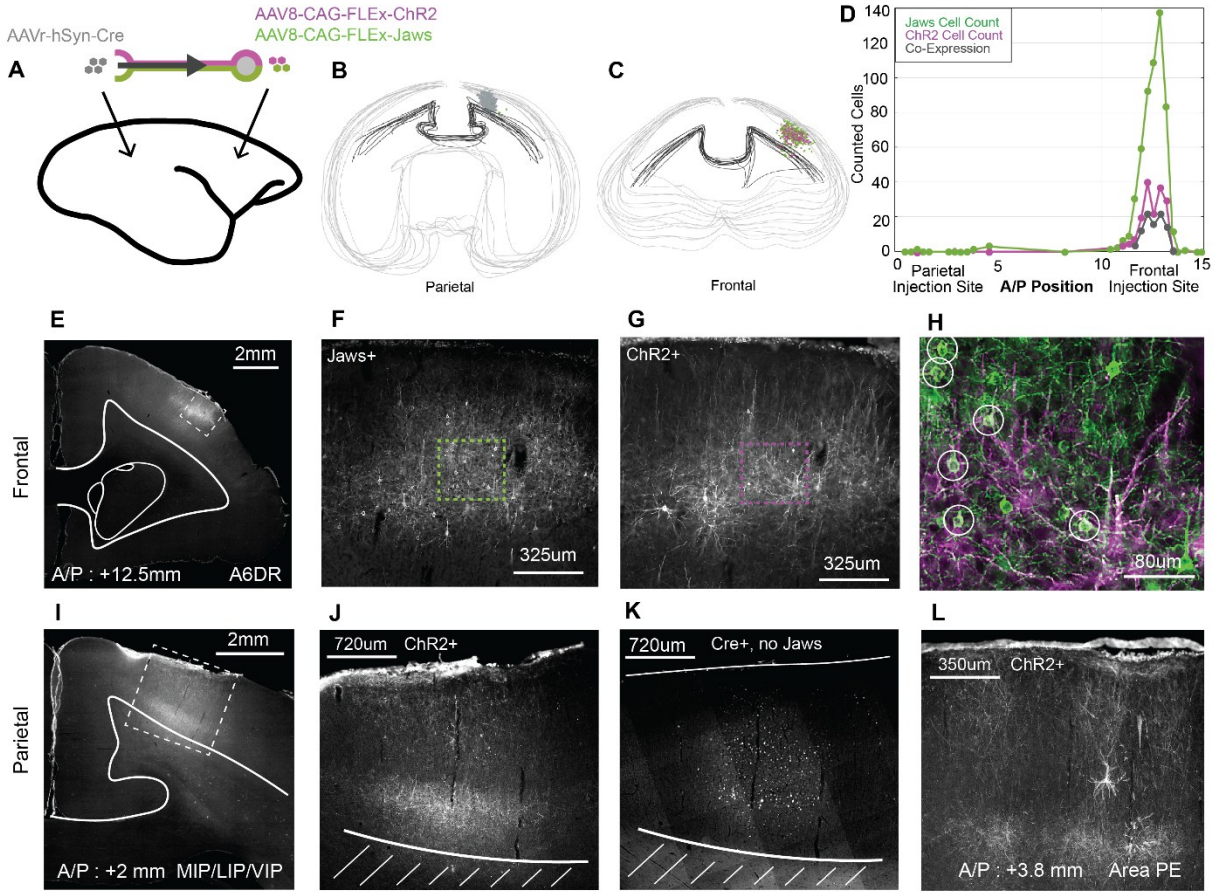

Figure 5. Efficient and Specific Premotor-Parietal Intersectional Expression of ChR2 and Jaws using AAV8

Figure 5. Efficient and Specific Premotor-Parietal Intersectional Expression of ChR2 and Jaws using AAV8

A Intersection viruses were delivered to parietal (AAVretro-Cre) and premotor (AAV8-ChR2 + AAV8-Jaws) marmoset cortex. **B-C** Illustration of cell counting with drawn brain perimeter and corpus callosum for each counted section. **D** Summary of manual soma cell counting over coronal sections. Each section was counted for Jaws expression, ChR2+ expression, and co-expression. Each dot represents a counted section. **E** Example section at premotor injection center showing Jaws+ cell bodies. **F,G** Zoom from E with Jaws+ and ChR2+ cell bodies. **H** Two channel overlay from zoom of the area highlighted in F,G with white circles indicating co-expression. **I** Example section at parietal injection center showing ChR2 terminals. **J** Zoom in from I: Abundant ChR2+ terminals in deep and superficial layers. Lines indicate the cortical surface and white matter. **K** Zoom from I: Cre+ cell labelling but notably without any Jaws+ axons from an anti-GFP/anti-BFP antibody stain. **L** Another anterior parietal example showing more ChR2+ terminals but no Jaws+ terminals, and one cell body reflecting leaky labeling.

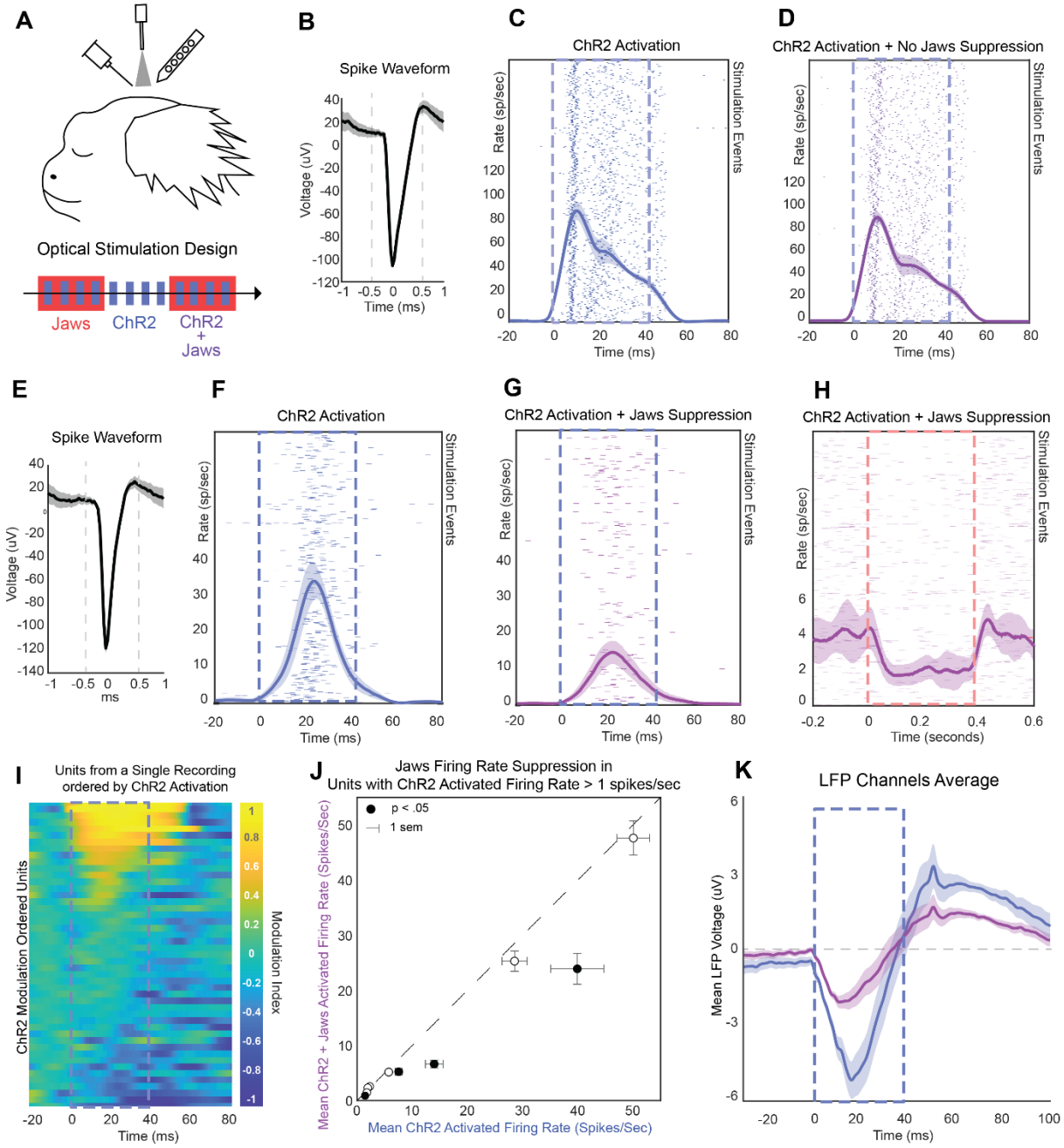

Figure 6. Excitation and Inhibition of Projection Neurons via Intersectional Co-Expression of ChR2 and Jaws

Figure 6. Excitation and Inhibition of Projection Neurons via Intersectional Co-Expression of ChR2 and Jaws

A Optogenetic tests were conducted in the anaesthetized marmoset. Histological data from this animal are shown in Figure 5. Optical stimulation consisted of ChR2 stimulation pulses (in blue, bottom inset) or when overlapping with longer duration Jaws stimulation pulses (in red). **B-D** The spike waveform of an isolated single unit, showing ChR2 stimulation (in blue) and relatively little suppression of the ChR2 response during concomitant Jaws stimulation (in purple). **E-G** A second example unit shown in the same format as B-D, with this unit showing suppression of the ChR2 response during concomitant Jaws stimulation. **H** On a longer time scale, the 400 ms pulse of the Jaws laser shows significant suppression in baseline firing rate for this example unit. **I** The modulation of firing rate in response to ChR2 stimulation shown in color scale (yellow-excitatation, blue – suppression) shown across the population of units sorted by ChR2 modulation. **J** Mean ChR2 pulse triggered firing rate plotted against mean ChR2 + Jaws firing rate for units demonstrating a firing rate increase greater than 1Hz with ChR2 stimulation. **K** Mean population LFP traces for ChR2 and ChR2+Jaws stimulation show a 59% reduction by Jaws at peak deflection.

SUPPLEMENTAL FIGURES

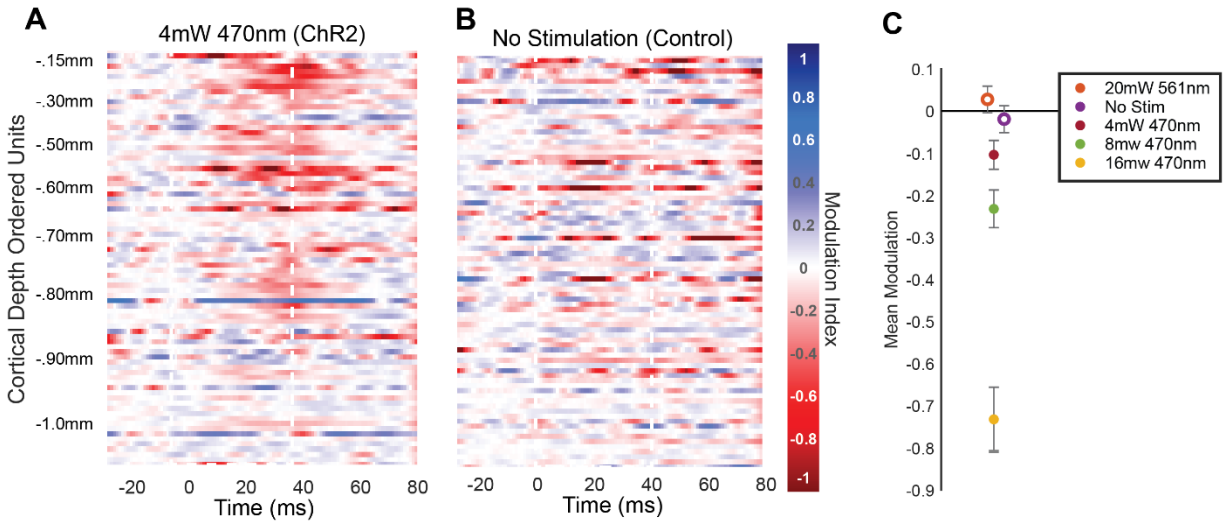

Supplemental Figure 1. Controlling Laser Power Effects in Awake mDlx-ChR2 Optogenetic Studies in the Marmoset

A Modulation scores of units ordered by cortical depth in an additional 4mW laser power condition to those shown in **Figure 1 L-N**. **B** No stimulation-triggered "events" were randomly selected from periods in between runs of laser stimulation. **C** Mean modulation scores were calculated for each condition over the population of units during the laser stimulation window. Error bars indicate 2x SEM. Closed circles indicate $p<.05$ from a simple one sample students t-test. See **Figure 1 L-N**.

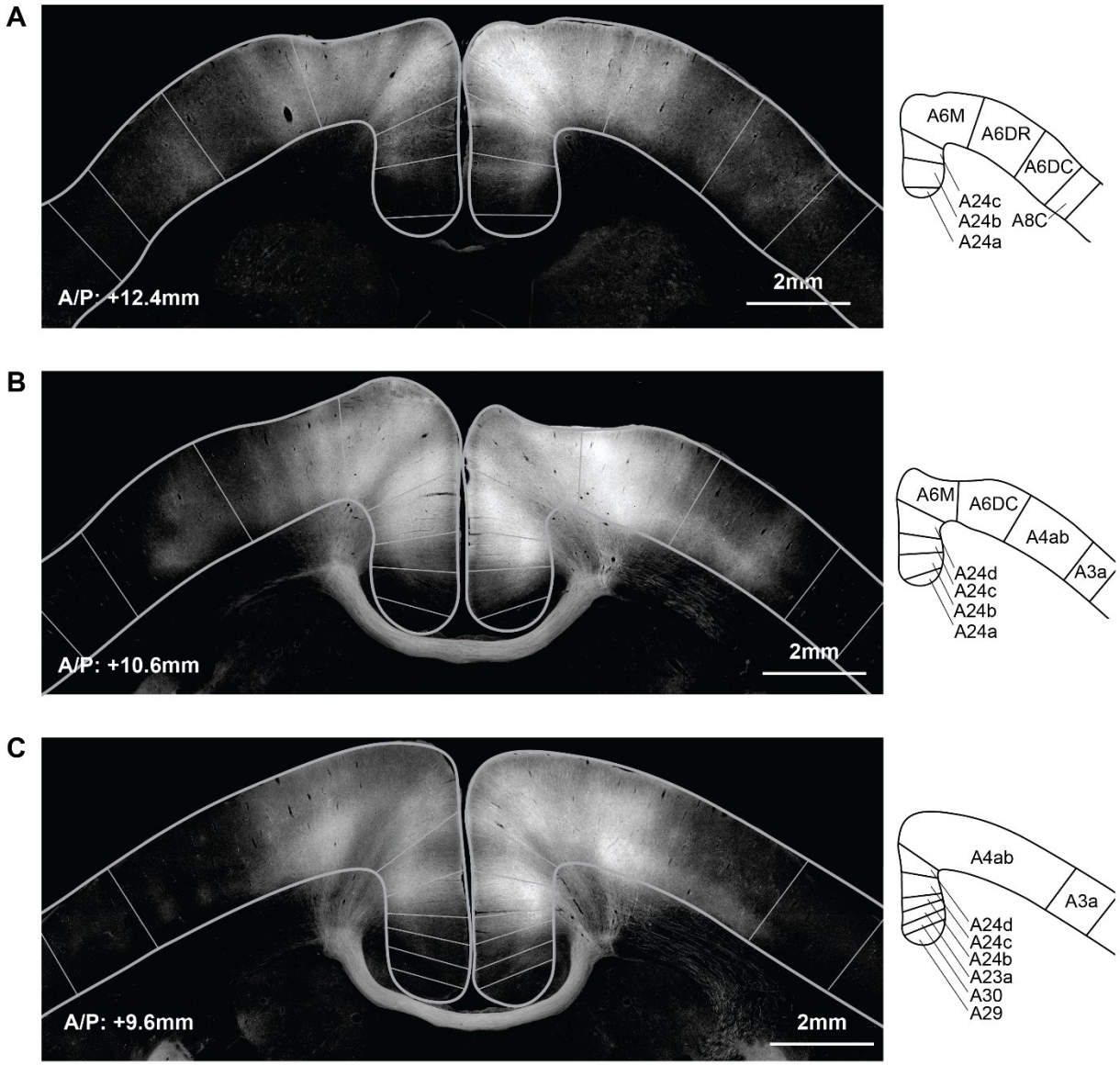

Supplemental Figure 2. Symmetrical and Patchy Patterns of Cortical Expression in Cross-Callosal Intersectional Expression of ChR2 Using AAV9

A-C Intersectional ChR2 expression in three sections sampled along the anterior/posterior axis. AAVretro-hSyn-Cre was injected into left cortex and AAV9-CAG-FLEx-ChR2 was injected into right cortex according to **Figure 2**. Grey outlines correspond to illustrations in the right column, which are adapted from the Paxino's Marmoset Brain Atlas, 2012. The general patterns of expression in each section are not homogeneous reflecting multiple injections per site, with patchy columns of expression vertically striating cortex, and symmetry across the midline. It is also apparent in **B** and **C** that labelling extends laterally in right cortex to deep layers more so than in superficial layers.

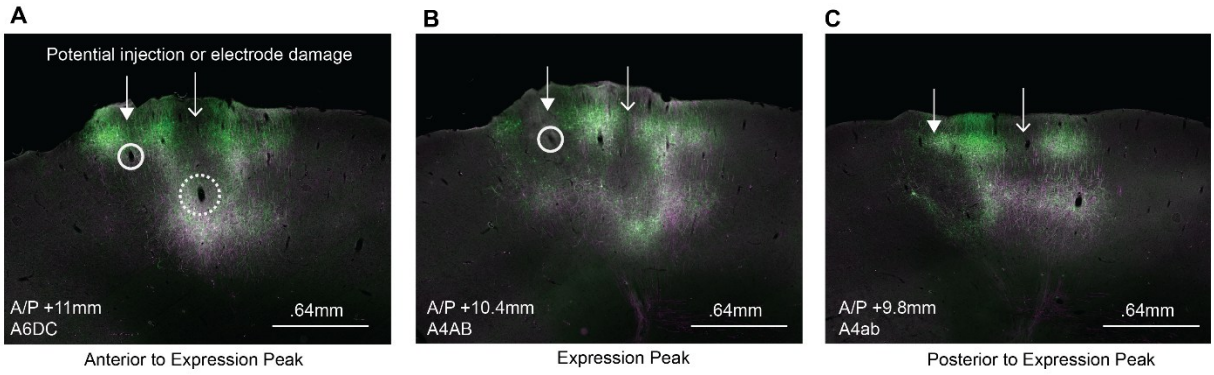

Supplemental Figure 3. Complex Expression Patterns in Intersectional Cross-Callosal Expression using AAV8.

A-C Sequential coronal sections from the cross-callosal AAV8 intersection showing the correspondence of expression shadows (arrows) with underlying vasculature (circles), which could have been ruptured by electrode shanks or the injection pipette. See **Figure 4C**.

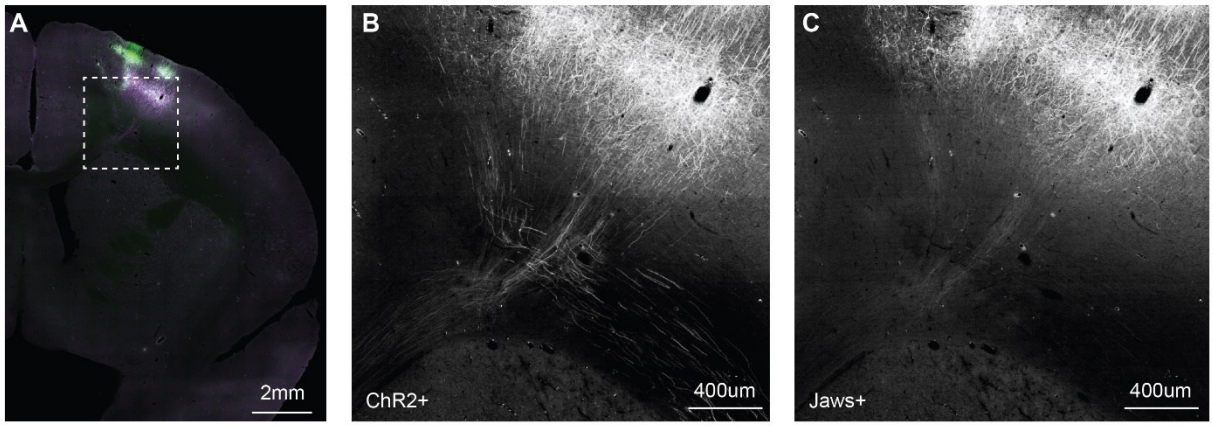

Supplemental Figure 4. ChR2 Demonstrates More Robust Axonal Labeling than Jaws

A Overview of coronal section labelled with ChR2 and Jaws. The dashed box, which contains lateral corpus callosum and dorsal internal capsule, is separated into color channels in **B** and **C**. **B** ChR2 labelling shows robust axonal labelling in projections from the injection site. **C** Jaws shows weak axonal labelling in comparison to ChR2. See **Figure 4**.

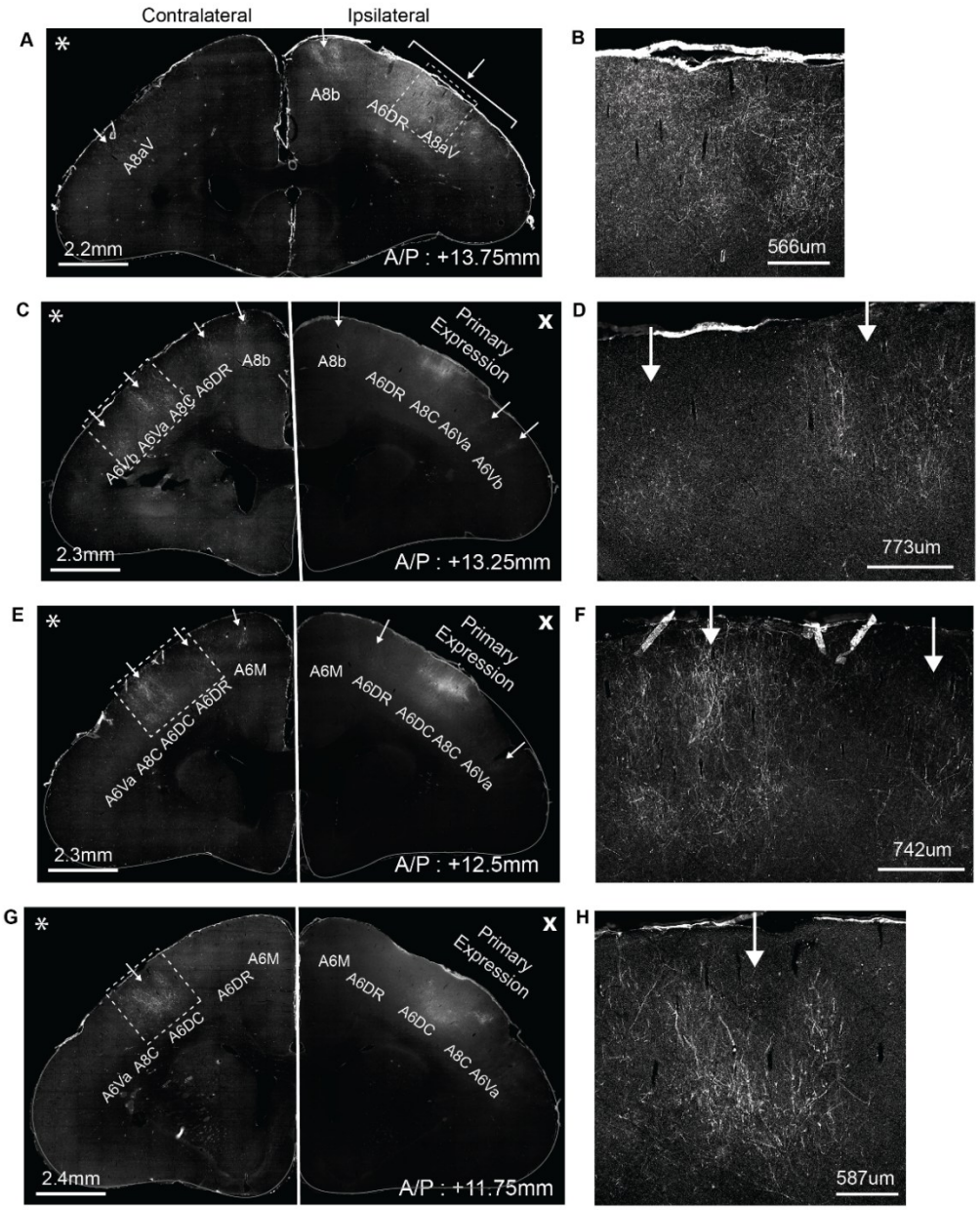

Supplemental Figure 5. Ipsilateral Premotor-Parietal Projections Neurons Send Frontal and Contralateral Collaterals.

All images depict RFP antibody stain enhanced ChR2 labelling from the ipsilateral intersection expression in **Figure 5**. The right column of images are zoom-ins of the dashed rectangles in the left column overviews. Arrows indicate clusters of axon terminals. Panels **C, E, G** are split to emphasize the low expression intensity terminals (*) while keeping high levels of primary expression in imaging range (x). **A-B** This section anterior to the injection site shows ipsilateral terminals and a small patch of contralateral terminals in A8aV. **C-D** Contralateral terminal patches are evident in A6a/b, A8C, A6DR, and A8b. **E-F** Contralateral terminal patches are evident in A6DR, A6DC, and A6M. **G-H** Contralateral terminals are evident in a main patch in A6DC.

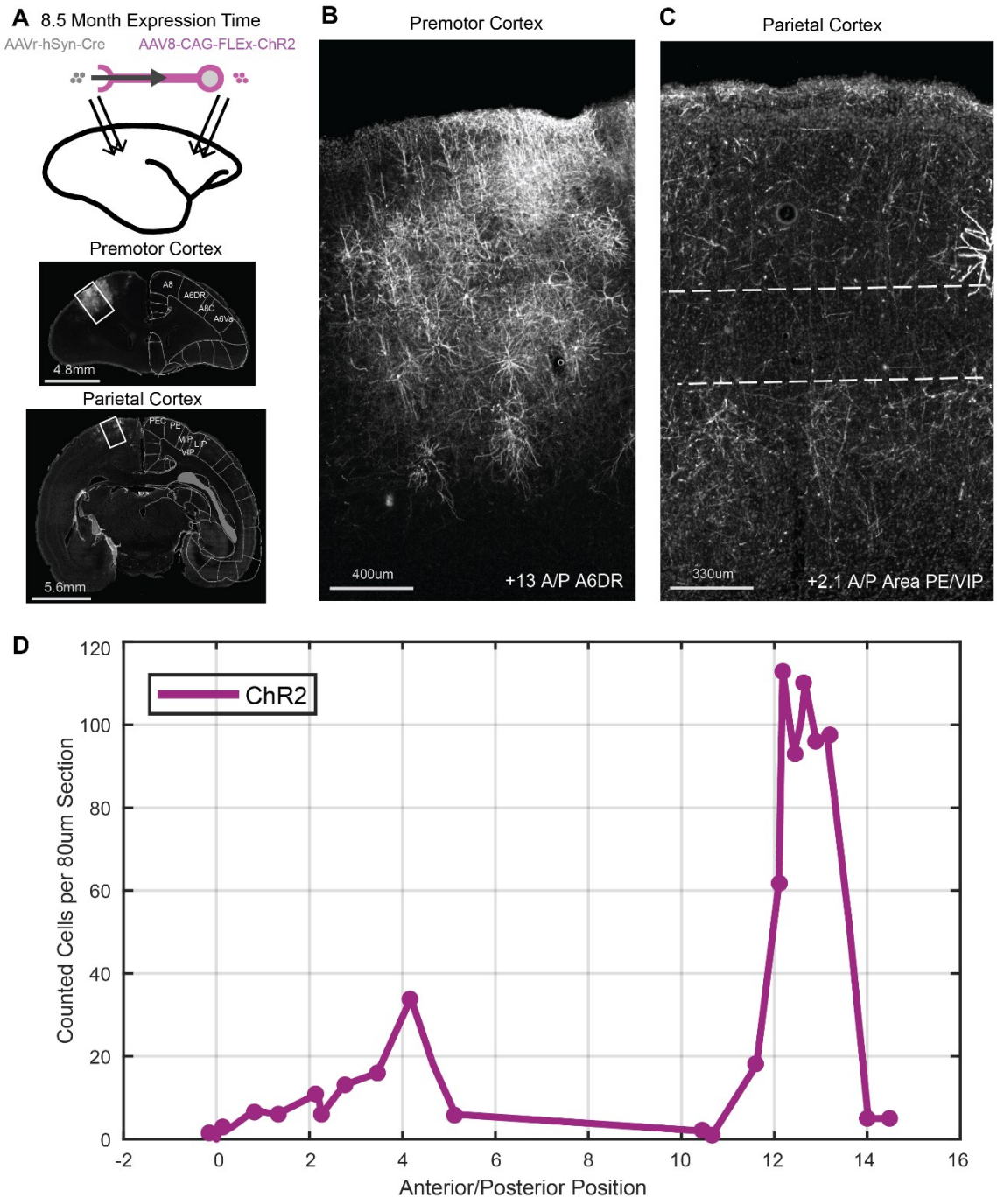

Supplemental Figure 6. Long Duration Expression of ChR2 in Intersectional Premotor-Parietal Cortex using AAV8

A Methods for this experiment are the same as described in **Figure 5**, except that ChR2 was injected without Jaws. **B-D** After 8.5 months of expression incubation, histology and manual cell counting were performed. Full cell membrane labelling is evident without signs of over-expression. Axons are evident in deep and superficial layers of parietal cortex.

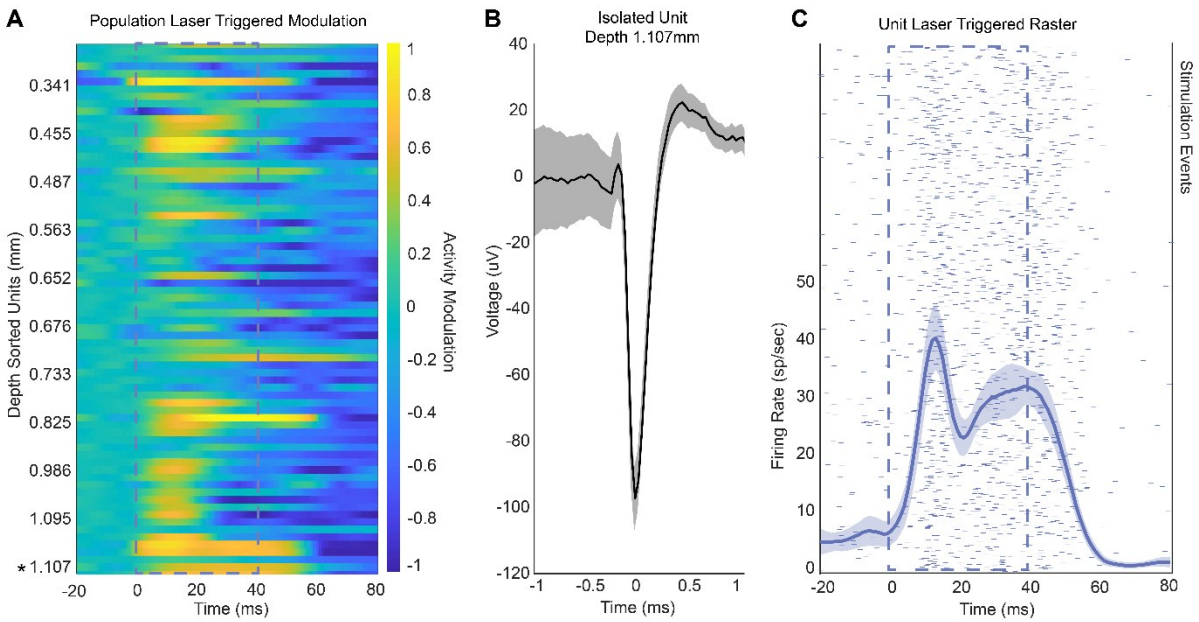

Supplemental Figure 7. Depth Profile of Intersection-Labeled Units Modulated by ChR2 Stimulation.

A The modulation of firing rate in response to ChR2 stimulation shown in color scale (yellow-excitatation, blue – suppression) shown across the population of units sorted by the depth of the recording site. Data are from a second sampled neural population from the same experiment as shown in Figure 6I. Depth is estimated from the localization of the unit along the array of electrodes. The spiking waveform and light-triggered firing rate response of the deepest unit, found at 1.107 mm relative to the electrode array (*), are illustrated in **B** and **C**, respectively. This demonstrates that excitation was possible from blue light at the cortical surface at depths up to 1.1mm.